ELSEVIER

Nuclear Physics B 421 (1994) 3–37

NUCLEAR PHYSICS B

Search for the standard model Higgs boson in Z^0 decays

DELPHI Collaboration

P. Abreu [t], W. Adam [g], T. Adye [ak], E. Agasi [ad], I. Ajinenko [ap], R. Aleksan [am], G.D. Alekseev [n], P.P. Allport [u], S. Almehed [w], F.M.L. Almeida [au], S.J. Alvsvaag [d], U. Amaldi [g], A. Andreazza [aa], P. Antilogus [x], W-D. Apel [o], R.J. Apsimon [ak], Y. Arnoud [am], B. Åsman [ar], J-E. Augustin [r], A. Augustinus [ad], P. Baillon [g], P. Bambade [r], F. Barao [t], R. Barate [ℓ], G. Barbiellini [at], D.Y. Bardin [n], G.J. Barker [ah], A. Baroncelli [an], O. Barring [g], J.A. Barrio [y], W. Bartl [ay], M.J. Bates [ak], M. Battaglia [m], M. Baubillier [v], K-H. Becks [ba], M. Begalli [aj], P. Beilliere [f], P. Beltran [i], A.C. Benvenuti [e], M. Berggren [ao], D. Bertrand [b], F. Bianchi [as], M. Bigi [as], M.S. Bilenky [n], P. Billoir [v], J. Bjarne [w], D. Bloch [h], J. Blocki [az], S. Blyth [ah], V. Bocci [aℓ], P.N. Bogolubov [n], T. Bolognese [am], M. Bonesini [aa], W. Bonivento [aa], P.S.L. Booth [u], G. Borisov [ap], C. Bosio [an], B. Bostjancic [aq], S. Bosworth [ah], O. Botner [av], E. Boudinov [ap], B. Bouquet [r], C. Bourdarios [r], T.J.V. Bowcock [u], M. Bozzo [k], S. Braibant [b], P. Branchini [an], K.D. Brand [ai], R.A. Brenner [m], H. Briand [v], C. Bricman [b], L. Brillault [v], R.C.A. Brown [g], J-M. Brunet [f], L. Bugge [af], T. Buran [af], A. Buys [g], J.A.M.A. Buytaert [g], M. Caccia [aa], M. Calvi [aa], A.J. Camacho Rozas [ao], R. Campion [u], T. Camporesi [g], V. Canale [aℓ], K. Cankocak [ar], F. Cao [b], F. Carena [g], P. Carrilho [au], L. Carroll [u], R. Cases [aw], C. Caso [k], M.V. Castillo Gimenez [aw], A. Cattai [g], F.R. Cavallo [e], L. Cerrito [aℓ], V. Chabaud [g], A. Chan [a], M. Chapkin [ap], Ph. Charpentier [g], J. Chauveau [v], P. Checchia [ai], G.A. Chelkov [n], L. Chevalier [am], P. Chliapnikov [ap], V. Chorowicz [v], J.T.M. Chrin [aw], V. Cindro [aq], P. Collins [ah], J.L. Contreras [r], R. Contri [k], E. Cortina [aw], G. Cosme [r], F. Couchot [r], H.B. Crawley [a], D. Crennell [ak], G. Crosetti [k], J. Cuevas Maestro [ag], S. Czellar [m], E. Dahl-Jensen [ab],

SSDI 0550-3213(94)00175-E

J. Dahm[ba], B. Dalmagne[r], M. Dam[af], G. Damgaard[ab], E. Daubie[b], A. Daum[o], P.D. Dauncey[g], M. Davenport[g], J. Davies[u], W. Da Silva[v], C. Defoix[f], P. Delpierre[z], N. Demaria[ah], A. De Angelis[g], H. De Boeck[b], W. De Boer[o], S. De Brabandere[b], C. De Clercq[b], M.D.M. De Fez Laso[aw], C. De La Vaissiere[v], B. De Lotto[at], A. De Min[aa], L. De Paula[au], H. Dijkstra[g], L. Di Ciaccio[aℓ], F. Djama[h], J. Dolbeau[f], M. Donszelmann[g], K. Doroba[az], M. Dracos[h], J. Drees[ba], M. Dris[ae], Y. Dufour[g], F. Dupont[ℓ], D. Edsall[a], R. Ehret[o], T. Ekelof[av], G. Ekspong[ar], M. Elsing[ba], J-P. Engel[h], N. Ershaidat[v], M. Espirito Santo[t], D. Fassouliotis[ae], M. Feindt[g], A. Ferrer[aw], T.A. Filippas[ae], A. Firestone[a], H. Foeth[g], E. Fokitis[ae], F. Fontanelli[k], F. Formenti[g], J-L. Fousset[z], S. Francon[x], B. Franek[ak], P. Frenkiel[f], D.C. Fries[o], A.G. Frodesen[d], R. Fruhwirth[ay], F. Fulda-Quenzer[r], H. Furstenau[g], J. Fuster[g], D. Gamba[as], M. Gandelman[q], C. Garcia[aw], J. Garcia[ao], C. Gaspar[g], U. Gasparini[ai], Ph. Gavillet[g], E.N. Gazis[ae], D. Gele[h], J-P. Gerber[h], P. Giacomelli[g], D. Gillespie[g], R. Gokieli[az], B. Golob[aq], V.M. Golovatyuk[n], J.J. Gomez Y Cadenas[g], G. Gopal[ak], L. Gorn[a], M. Gorski[az], V. Gracco[k], F. Grard[b], E. Graziani[an], G. Grosdidier[r], P. Gunnarsson[ar], J. Guy[ak], U. Haedinger[o], F. Hahn[ba], M. Hahn[ar], S. Hahn[ba], S. Haider[ad], Z. Hajduk[p], A. Hakansson[w], A. Hallgren[av], K. Hamacher[ba], G. Hamel De Monchenault[am], W. Hao[ad], F.J. Harris[ah], V. Hedberg[w], R. Henriques[t], J.J. Hernandez[aw], J.A. Hernando[aw], P. Herquet[b], H. Herr[g], T.L. Hessing[u], E. Higon[aw], H.J. Hilke[g], T.S. Hill[a], S-O. Holmgren[ar], P.J. Holt[ah], D. Holthuizen[ad], P.F. Honore[f], M. Houlden[u], J. Hrubec[ay], K. Huet[b], K. Hultqvist[ar], P. Ioannou[c], P-S. Iversen[d], J.N. Jackson[u], R. Jacobsson[ar], P. Jalocha[p], G. Jarlskog[w], P. Jarry[am], B. Jean-Marie[r], E.K. Johansson[ar], M. Jonker[g], L. Jonsson[w], P. Juillot[h], M. Kaiser[o], G. Kalmus[ak], F. Kapusta[v], M. Karlsson[ar], E. Karvelas[i], S. Katsanevas[c], E.C. Katsoufis[ae], R. Keranen[g], B.A. Khomenko[n], N.N. Khovanski[n], B. King[u], N.J. Kjaer[ab], H. Klein[g], A. Klovning[d], P. Kluit[ad], A. Koch-Mehrin[ba], J.H. Koehne[o], B. Koene[ad], P. Kokkinias[i], M. Koratzinos[af], K. Korcyl[p], A.V. Korytov[n], V. Kostioukhine[ap], C. Kourkoumelis[c], O. Kouznetsov[n], P.H. Kramer[ba], M. Krammer[ay], C. Kreuter[o], J. Krolikowski[az], I. Kronkvist[w], W. Krupinski[p], K. Kulka[av], K. Kurvinen[m], C. Lacasta[aw], C. Lambropoulos[i], J.W. Lamsa[a], L. Lanceri[at], P. Langefeld[ba], V. Lapin[ap], I. Last[u], J-P. Laugier[am], R. Lauhakangas[m], G. Leder[ay], F. Ledroit[ℓ], R. Leitner[ac], Y. Lemoigne[am], J. Lemonne[b], G. Lenzen[ba],

V. Lepeltier[r], T. Lesiak[p], J.M. Levy[h], E. Lieb[ba], D. Liko[ay], R. Lindner[ba], A. Lipniacka[r], I. Lippi[ai], B. Loerstad[w], M. Lokajicek[j], J.G. Loken[ah], A. Lopez-Fernandez[g], M.A. Lopez Aguera[ao], M. Los[ad], D. Loukas[i], J.J. Lozano[aw], P. Lutz[f], L. Lyons[ah], G. Maehlum[o], J. Maillard[f], A. Maio[t], A. Maltezos[i], F. Mandl[ay], J. Marco[ao], B. Marechal[au], M. Margoni[ai], J-C. Marin[g], C. Mariotti[an], A. Markou[i], T. Maron[ba], S. Marti[aw], C. Martinez-Rivero[ao], F. Martinez-Vidal[aw], F. Matorras[ao], C. Matteuzzi[aa], G. Matthiae[aℓ], M. Mazzucato[ai], M. Mc Cubbin[u], R. Mc Kay[a], R. Mc Nulty[u], J. Medbo[av], C. Meroni[aa], W.T. Meyer[a], M. Michelotto[ai], E. Migliore[as], I. Mikulec[ay], L. Mirabito[x], W.A. Mitaroff[ay], G.V. Mitselmakher[n], U. Mjoernmark[w], T. Moa[ar], R. Moeller[ab], K. Moenig[g], M.R. Monge[k], P. Morettini[k], H. Mueller[o], W.J. Murray[ak], B. Muryn[p], G. Myatt[ah], F. Naraghi[ℓ], F.L. Navarria[e], P. Negri[aa], S. Nemecek[j], W. Neumann[ba], N. Neumeister[ay], R. Nicolaidou[c], B.S. Nielsen[ab], V. Nikolaenko[ap], P.E.S. Nilsen[d], P. Niss[ar], A. Nomerotski[ai], A. Normand[ah], V. Obraztsov[ap], A.G. Olshevski[n], R. Orava[m], K. Osterberg[m], A. Ouraou[am], P. Paganini[r], M. Paganoni[aa], R. Pain[v], H. Palka[p], Th.D. Papadopoulou[ae], L. Pape[g], F. Parodi[k], A. Passeri[an], M. Pegoraro[ai], J. Pennanen[m], L. Peralta[t], H. Pernegger[ay], M. Pernicka[ay], A. Perrotta[e], C. Petridou[at], A. Petrolini[k], H.T. Phillips[ak], G. Piana[k], F. Pierre[am], M. Pimenta[t], S. Plaszczynski[r], O. Podobrin[o], M.E. Pol[q], G. Polok[p], P. Poropat[at], V. Pozdniakov[n], M. Prest[at], P. Privitera[aℓ], A. Pullia[aa], D. Radojicic[ah], S. Ragazzi[aa], H. Rahmani[ae], J. Rames[j], P.N. Ratoff[s], A.L. Read[af], M. Reale[ba], P. Rebecchi[r], N.G. Redaelli[aa], M. Regler[ay], D. Reid[g], P.B. Renton[ah], L.K. Resvanis[c], F. Richard[r], J. Richardson[u], J. Ridky[j], G. Rinaudo[as], A. Romero[as], I. Roncagliolo[k], P. Ronchese[ai], L. Roos[ℓ], E.I. Rosenberg[a], E. Rosso[g], P. Roudeau[r], T. Rovelli[e], W. Ruckstuhl[ad], V. Ruhlmann-Kleider[am], A. Ruiz[ao], K. Rybicki[p], H. Saarikko[m], Y. Sacquin[am], G. Sajot[ℓ], J. Salt[aw], J. Sanchez[y], M. Sannino[k], S. Schael[g], H. Schneider[o], M.A.E. Schyns[ba], G. Sciolla[as], F. Scuri[at], A.M. Segar[ah], A. Seitz[o], R. Sekulin[ak], M. Sessa[at], R. Seufert[o], R.C. Shellard[aj], I. Siccama[ad], P. Siegrist[am], S. Simonetti[k], F. Simonetto[ai], A.N. Sisakian[n], G. Skjevling[af], G. Smadja[x], N. Smirnov[ap], O. Smirnova[n], G.R. Smith[ak], R. Sosnowski[az], D. Souza-Santos[aj], T. Spassov[t], E. Spiriti[an], S. Squarcia[k], H. Staeck[ba], C. Stanescu[an], S. Stapnes[af], I. Stavitski[ai], G. Stavropoulos[i], K. Stepaniak[az], F. Stichelbaut[g],

A. Stocchi [r], J. Straver [g], R. Strub [h], B. Stugu [d], M. Szczekowski [az], M. Szeptycka [az], T. Tabarelli [aa], O. Tchikilev [ap], G.E. Theodosiou [i], Z. Thome [au], A. Tilquin [z], J. Timmermans [ad], V.G. Timofeev [n], L.G. Tkatchev [n], T. Todorov [h], D.Z. Toet [ad], A. Tomaradze [b], B. Tome [t], E. Torassa [as], L. Tortora [an], D. Treille [g], W. Trischuk [g], G. Tristram [f], C. Troncon [aa], A. Tsirou [g], E.N. Tsyganov [n], M. Turala [p], M-L. Turluer [am], T. Tuuva [m], I.A. Tyapkin [v], M. Tyndel [ak], S. Tzamarias [u], B. Ueberschaer [ba], S. Ueberschaer [ba], O. Ullaland [g], V. Uvarov [ap], G. Valenti [e], E. Vallazza [g], J.A. Valls Ferrer [aw], C. Vander Velde [b], G.W. Van Apeldoorn [ad], P. Van Dam [ad], M. Van Der Heijden [ad], W.K. Van Doninck [b], J. Van Eldik [ad], P. Vaz [g], G. Vegni [aa], L. Ventura [ai], W. Venus [ak], F. Verbeure [b], M. Verlato [ai], L.S. Vertogradov [n], D. Vilanova [am], P. Vincent [x], L. Vitale [at], E. Vlasov [ap], A.S. Vodopyanov [n], M. Vollmer [ba], M. Voutilainen [m], V. Vrba [j], H. Wahlen [ba], C. Walck [ar], F. Waldner [at], A. Wehr [ba], M. Weierstall [ba], P. Weilhammer [g], A.M. Wetherell [g], J.H. Wickens [b], M. Wielers [o], G.R. Wilkinson [ah], W.S.C. Williams [ah], M. Winter [h], M. Witek [g], G. Wormser [r], K. Woschnagg [av], K. Yip [ah], O. Yushchenko [ap], A. Zaitsev [ap], A. Zalewska [p], P. Zalewski [az], D. Zavrtanik [aq], E. Zevgolatakos [i], N.I. Zimin [n], M. Zito [am], D. Zontar [aq], R. Zuberi [ah], G. Zumerle [ai]

[a] *Ames Laboratory and Department of Physics, Iowa State University, Ames IA 50011, USA*

[b] *Physics Department, Univ. Instelling Antwerpen, Universiteitsplein 1, B-2610 Wilrijk, Belgium and IIHE, ULB-VUB, Pleinlaan 2, B-1050 Brussels, Belgium and Faculté des Sciences, Univ. de l'Etat Mons, Av. Maistriau 19, B-7000 Mons, Belgium*

[c] *Physics Laboratory, University of Athens, Solonos Str. 104, GR-10680 Athens, Greece*

[d] *Department of Physics, University of Bergen, Allégaten 55, N-5007 Bergen, Norway*

[e] *Dipartimento di Fisica, Università di Bologna and INFN, Via Irnerio 46, I-40126 Bologna, Italy*

[f] *Collège de France, Lab. de Physique Corpusculaire, IN2P3-CNRS, F-75231 Paris Cedex 05, France*

[g] *CERN, CH-1211 Geneva 23, Switzerland*

[h] *Centre de Recherche Nucléaire, IN2P3 - CNRS/ULP - BP20, F-67037 Strasbourg Cedex, France*

[i] *Institute of Nuclear Physics, N.C.S.R. Demokritos, P.O. Box 60228, GR-15310 Athens, Greece*

[j] *FZU, Inst. of Physics of the C.A.S. High Energy Physics Division, Na Slovance 2, CS-180 40, Prague 8, Czech Republic*

[k] *Dipartimento di Fisica, Università di Genova and INFN, Via Dodecaneso 33, I-16146 Genova, Italy*

[ℓ] *Institut des Sciences Nucléaires, IN2P3-CNRS, Université de Grenoble 1, F-38026 Grenoble, France*

[m] *Research Institute for High Energy Physics, SEFT, P.O. Box 9, FIN-00014 University of Helsinki, Finland*

[n] *Joint Institute for Nuclear Research, Dubna, Head Post Office, P.O. Box 79, 101 000 Moscow, Russian Federation*

[o] *Institut für Experimentelle Kernphysik, Universität Karlsruhe, Postfach 6980, D-76128 Karlsruhe, Germany*

[p] *High Energy Physics Laboratory, Institute of Nuclear Physics, Ul. Kawiory 26a, PL-30055 Krakow 30, Poland*

[q] *Centro Brasileiro de Pesquisas Físicas, rua Xavier Sigaud 150, RJ-22290 Rio de Janeiro, Brazil*

[r] *Université de Paris-Sud, Lab. de l'Accélérateur Linéaire, IN2P3-CNRS, Bat 200, F-91405 Orsay, France*

[s] *School of Physics and Materials, University of Lancaster, Lancaster LA1 4YB, UK*

[t] LIP, IST, FCUL - Av. Elias Garcia, 14-1o, P-1000 Lisbon Codex, Portugal
[u] Department of Physics, University of Liverpool, P.O. Box 147, Liverpool L69 3BX, UK
[v] LPNHE, IN2P3-CNRS, Universités Paris VI et VII, Tour 33 (RdC), 4 place Jussieu, F-75252 Paris Cedex 05, France
[w] Department of Physics, University of Lund, Sölvegatan 14, S-22363 Lund, Sweden
[x] Université Claude Bernard de Lyon, IPNL, IN2P3-CNRS, F-69622 Villeurbanne Cedex, France
[y] Universidad Complutense, Avda. Complutense s/n, E-28040 Madrid, Spain
[z] Univ. d'Aix - Marseille II - CPP, IN2P3-CNRS, F-13288 Marseille Cedex 09, France
[aa] Dipartimento di Fisica, Università di Milano and INFN, Via Celoria 16, I-20133 Milan, Italy
[ab] Niels Bohr Institute, Blegdamsvej 17, DK-2100 Copenhagen 0, Denmark
[ac] NC, Nuclear Centre of MFF, Charles University, Areal MFF, V Holesovickach 2, CS-180 00, Prague 8, Czech Republic
[ad] NIKHEF-H, Postbus 41882, NL-1009 DB Amsterdam, The Netherlands
[ae] National Technical University, Physics Department, Zografou Campus, GR-15773 Athens, Greece
[af] Physics Department, University of Oslo, Blindern, N-1000 Oslo 3, Norway
[ag] Dpto. Fisica, Univ. Oviedo, C/P.Jimenez Casas, S/N-33006 Oviedo, Spain
[ah] Department of Physics, University of Oxford, Keble Road, Oxford OX1 3RH, UK
[ai] Dipartimento di Fisica, Università di Padova and INFN, Via Marzolo 8, I-35131 Padua, Italy
[aj] Depto. de Fisica, Pontificia Univ. Católica, C.P. 38071 RJ-22453 Rio de Janeiro, Brazil
[ak] Rutherford Appleton Laboratory, Chilton, Didcot OX11 OQX, UK
[al] Dipartimento di Fisica, Università di Roma II and INFN, Tor Vergata, I-00173 Rome, Italy
[am] Centre d'Etude de Saclay, DSM/DAPNIA, F-91191 Gif-sur-Yvette Cedex, France
[an] Istituto Superiore di Sanità, Ist. Naz. di Fisica Nucl. (INFN), Viale Regina Elena 299, I-00161 Rome, Italy
[ao] C.E.A.F.M., C.S.I.C. - Univ. Cantabria, Avda. los Castros, S/N-39006 Santander, Spain
[ap] Inst. for High Energy Physics, Serpukov P.O. Box 35, Protvino (Moscow Region), Russian Federation
[aq] J. Stefan Institute and Department of Physics, University of Ljubljana, Jamova 39, SI-61000 Ljubljana, Slovenia
[ar] Fysikum, Stockholm University, Box 6730, S-113 85 Stockholm, Sweden
[as] Dipartimento di Fisica Sperimentale, Università di Torino and INFN, Via P. Giuria 1, I-10125 Turin, Italy
[at] Dipartimento di Fisica, Università di Trieste and INFN, Via A. Valerio 2, I-34127 Trieste, Italy and Istituto di Fisica, Università di Udine, I-33100 Udine, Italy
[au] Univ. Federal do Rio de Janeiro, C.P. 68528 Cidade Univ., Ilha do Fundão, BR-21945-970 Rio de Janeiro, Brazil
[av] Department of Radiation Sciences, University of Uppsala, P.O. Box 535, S-751 21 Uppsala, Sweden
[aw] IFIC, Valencia-CSIC, and D.F.A.M.N., U. de Valencia, Avda. Dr. Moliner 50, E-46100 Burjassot (Valencia), Spain
[ay] Institut für Hochenergiephysik, Österr. Akad. d. Wissensch., Nikolsdorfergasse 18, A-1050 Vienna, Austria
[az] Inst. Nuclear Studies and University of Warsaw, Ul. Hoza 69, PL-00681 Warsaw, Poland
[ba] Fachbereich Physik, University of Wuppertal, Postfach 100 127, D-42097 Wuppertal 1, Germany

Received 21 March 1994; revised 20 April 1994; accepted 27 April 1994

Abstract

A search for the Standard Model Higgs boson was performed in the data sample of around 1 million hadronic Z^0 decays recorded in 1991 and 1992 with the DELPHI detector at LEP. The Higgs boson was searched for through its production in association with either neutrinos, electrons or muons. Four low mass events remain after the selections in the charged leptonic channels, that are likely to be due to background, especially four fermion processes. These results restrict the mass of the Standard Model Higgs boson to be larger than 55.7 GeV/c^2 at the 95% confidence level.

1. Introduction

This paper describes the search for the Standard Model Higgs boson in the data collected in 1991 and 1992 by the DELPHI detector at LEP.

The Higgs boson is searched for through its production in association with a virtual Z^0 boson, which subsequently decays into either neutrinos, electrons or muons. These three channels make only 26% of all possible production modes, but the corresponding final states can be disentangled from the background while keeping a reasonable efficiency. This is not the case in the two other modes with a Z^0 boson decaying into taus or hadrons. As our previous published result [1] excluded a Higgs boson with a mass up to 38 GeV/c^2, the present analysis is restricted to the high mass region, where the Higgs boson is expected to decay mainly into a $b\bar{b}$ pair. The final states to be selected are then characterized by a high hadronic multiplicity with either missing momentum or a pair of muons or electrons. Moreover, at high mass, the Higgs boson is expected to be weakly boosted so that the hadron system mostly splits into jets.

2. Data samples

The data sample recorded by DELPHI in 1991 and 1992 corresponds to an integrated luminosity of 34.6 pb^{-1}, i.e. to about 1 million hadronic Z^0 decays [2], which represents ten times the statistics of the 1990 data sample used in our previous publication on the same subject [1]. Updates of this result using the 1991 and 1992 data have already been reported in conferences [3,4]. The results of the other LEP experiments on the Higgs boson search can be found in Ref. [5].

The selection criteria are defined using simulated data samples of the Higgs particle production process [6] at masses ranging from 35 to 70 GeV/c^2 in 5 GeV/c^2 steps, and of the background contributions from hadronic Z^0 decays and from four fermion processes $e^+e^- \rightarrow \ell^+\ell^-q\bar{q}$ ($\ell = e, \mu, \tau$) [7]. The cross sections of the four fermion processes have been corrected by a factor 0.7 to take into account the initial state radiation which is not included in the generator. Non-dominant channel-dependent sources of background are also studied. They will be discussed in the corresponding sections.

The samples generated for the Higgs signal in each channel amount to 1000 events at each mass, except at 55 and 60 GeV/c^2 for which samples at least twice as big were generated. Two million hadronic Z^0 decays were generated, providing twice the statistics of the real data sample. Finally, the simulated samples of four fermion events with muons, electrons and taus in the final state amount to 5000, 5000, and 1250 events respectively, with an equal number of events per quark flavour. Given the different kinematical selections applied at the generation level in each channel to avoid divergences in the cross sections, these samples correspond to what is expected from $e^+e^-q\bar{q}$, $\mu^+\mu^-q\bar{q}$ and $\tau^+\tau^-q\bar{q}$ events with integrated luminosities 181, 44 and 7 times higher than the present one, respectively.

3. Experimental setup

The apparatus is described in detail in Ref. [8] which also gives the performance of the detector. In the following, we briefly mention the components which are relevant to the present analysis.

Tracks of charged particles are reconstructed in the inner detector, the time projection chamber and the outer detector in the barrel region. In the end caps, the reconstruction is achieved by the time projection chamber and the forward chambers. The microvertex detector provides additional precise points in the barrel region and is used to reconstruct precise secondary vertices and impact parameters. Neutral particle energies are measured in the electromagnetic and hadronic calorimeters. Muons are identified in three planes of drift chambers in the barrel region and two planes of drift chambers in the end caps.

As in any analysis dealing with missing energy, inefficient regions of the apparatus are important for the search in the neutrino channel. The three following regions deserve special care:

- The electromagnetic calorimeter has a 1.52° hole around 90° in the polar angle θ to lodge the central stiffening ring of the solenoid cryostat. Scintillator counters partially fill this gap and serve as a veto against photons.
- The barrel and forward parts of the electromagnetic calorimeter are not adjacent, to allow cable extraction. The corresponding θ range ($37° < \theta < 40.5°$ and $139.5° < \theta < 143°$) is covered only by the hadronic calorimeter.
- The tracking coverage is poor below 20°. Charged particles emitted at low angles are detected by the forward electromagnetic and hadronic calorimeters, and by the luminometer.

In the subsequent analysis, these weak regions will be defined by the following fiducial cuts in the polar angle θ:

- The "90° region" by a window of a few degrees (depending on the analysis) around 90°;
- The "40° region" by the following range in θ: $33° < \theta < 43°$ and $137° < \theta < 147°$;
- The "forward region" by a 30° or 15° cone (depending on the analysis) around the beam axis.

4. Neutrino channel

The Higgs boson production in association with neutrinos has the largest cross section of the three channels considered in this analysis. The experimental signature is a high mass unbalanced hadronic system, generally composed of two acollinear and acoplanar b-jets. The main background comes from hadronic Z^0 decays with missing energy and momentum due to particles escaping detection (neutrinos, long lived hadrons), and from bad energy reconstruction or particle losses in the regions of the apparatus with poor detector coverage. A large number of variables is necessary to reject this background. In such conditions, standard analysis methods based on sequential selections generally lead to a low efficiency. Two methods are used to improve the background suppression and the selection efficiency, both attempting to optimize the use of the discriminating

power of the analysis variables. Section 4.1 describes the results of the analysis with a neural network while section 4.2 is devoted to a probabilistic approach.

Both analyses use charged particles with momenta greater than 100 MeV/c and neutral particles with energies above 100 MeV to compute the selection variables, such as, for instance, the event invariant mass, the total transverse momentum with respect to the beam axis, global shape variables etc. These selected particles are also used to specify the jet content of the events. This is done in three ways. First, events are divided into two hemispheres with respect to the plane perpendicular to the thrust axis and the neutral and charged particles in each hemisphere are summed up to build what will be referred to as "hemispheric jets". A jet search is also performed using the cluster algorithm LUCLUS [9], with the minimum distance between two clusters, d_{join}, kept to its default value of 2.5 GeV/c. Jets resulting from this search will be referred to as "jets" with no other qualification. Finally, in order to check the event features in the three-jet topology the same cluster algorithm is also applied with a number of jets fixed to three.

4.1. Neural network analysis

A preselection is made in order to remove the bulk of the background and to feed the neural network with events in the region of the variable space that contains the signal. We first select events with an invariant mass between 20 GeV/c^2 and 70 GeV/c^2, at least five charged particles and a sphericity exceeding 0.02.

As a second step, events are kept if the acollinearity of the two hemispheric jets is greater than 8°, if the smallest angle between any jet and the missing momentum exceeds 15° and if the total energy carried by charged particles (hereafter referred to as total charged energy) is above 12 GeV.

As the Higgs boson is expected to decay predominantly into a $b\bar{b}$ pair, the microvertex detector can be used to discriminate against the background from Z^0 decays into light quarks (which represent 78% of the hadronic decays) by benefitting from the lifetime of the b-hadrons. The vertex detector coverage being about 70% of the full solid angle, the selected events are divided into subsamples with and without information in the vertex detector. To belong to the first sample, events are required to be in the acceptance of the vertex detector, namely the polar angle of the thrust axes in both hemispheres defined by the plane perpendicular to the event thrust axis must satisfy $|\cos\theta| < 0.65$. In addition, events must contain at least three tracks, each one with a minimum of two well associated hits in the vertex detector.

The two subsamples populate different angular regions of the detector. The sample with vertex detector information is largely contained in the barrel region, while the second sample is predominantly located in the forward regions. The amount of background in the two samples is different, resulting in different selections at some point in the analysis. Thus, in order to remove a small component of events with low total transverse momentum and with few charged particles, there is an additional preselection for the sample without vertex detector information which requires events to have more than 8 charged particles and a total charged energy greater than 17 GeV.

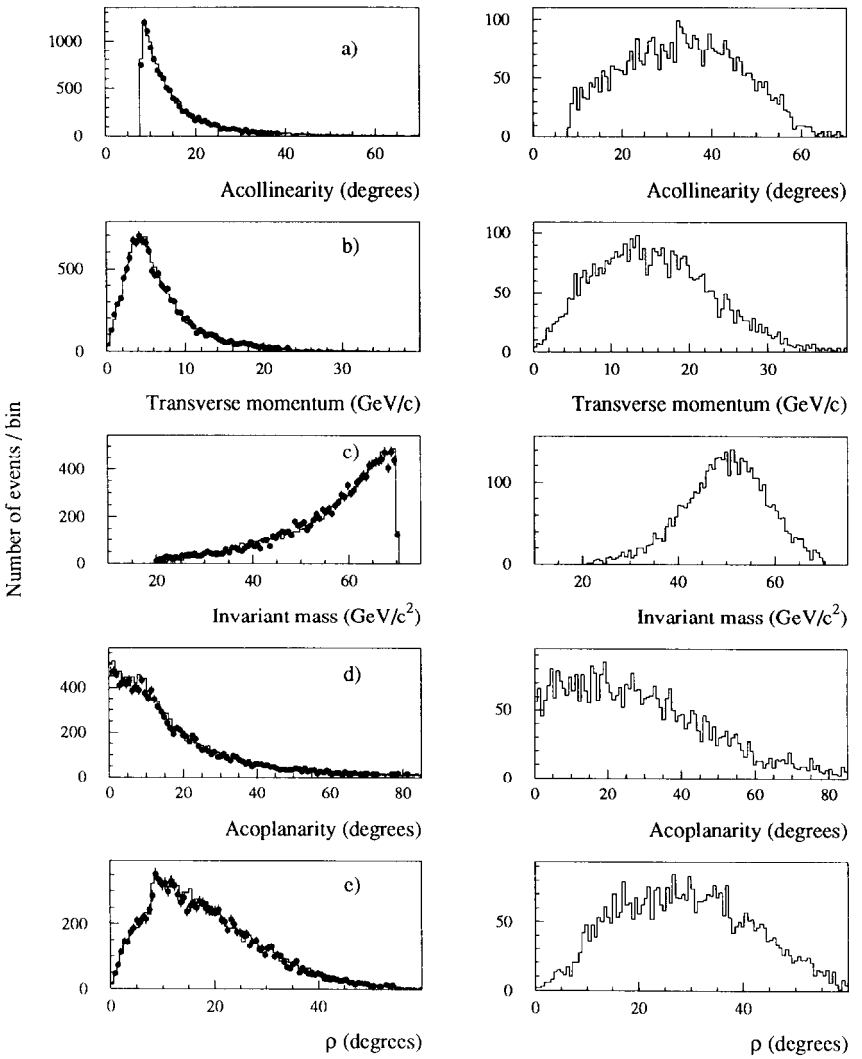

Fig. 1. Distributions of the main variables used in the neural network analysis of the neutrino channel. The preselections described in the text have been applied. Plots on the left show a comparison between real data (dots) and simulated $q\bar{q}$ events (solid line) normalised to the number of real data events. Plots on the right show the expected unnormalised distributions for a 55 GeV/c^2 Higgs boson.

The acceptance of the above selections for $H^0\nu\bar{\nu}$ events at 55 GeV/c^2 is 81.2%, while approximately 98.5% of the hadronic Z^0 decays are rejected. Fig. 1 shows a comparison between real data and simulated $q\bar{q}$ events at this stage of the analysis for a set of selected variables, defined in the next subsections. Both samples are normalised to the same number of events. The agreement is good. To illustrate the discriminating power

of the variables, the unnormalised distributions for a 55 GeV/c^2 Higgs boson are also shown.

4.1.1. The neural network

After the preselection, a neural network is used to distinguish signal events from the dominant $q\bar{q}$ background. The same network processes the samples with and without information in the vertex detector. It is of the feed-forward type with back-propagation of errors [10]. It has one input layer with 15 nodes and 2 intermediate layers with 8 and 3 nodes, respectively, which converge to the output node.

The network is trained to separate the signal from a 55 GeV/c^2 Higgs boson from the $Z^0 \rightarrow q\bar{q}(\gamma)$ background. To decide which variables to feed to the network a step-wise linear discriminant analysis is first performed which at each stage includes the variable seen to give the largest improvement in the discrimination. The network is then trained to give an output value close to one for signal events and close to zero for background events. The following variables, in the order given by the linear discriminant analysis, are used as input nodes in the neural network:

- The sum of the opening angles of the three pairs of jets when forcing three jets to be reconstructed;
- The energy carried by neutral particles (hereafter referred to as neutral energy) within 30° of the beam axis;
- The sum of the positive longitudinal momentum components along the second eigenvector of the sphericity tensor in the c.m.s. of the observed particles;
- The acollinearity between the two hemispheric jets (see Fig. 1a);
- The missing transverse momentum with respect to the beam axis (see Fig. 1b);
- The energy within 40° of the missing momentum direction;
- The charged energy within 30° of the beam axis;
- The total observed energy;
- The sum of the positive longitudinal momentum components along the sphericity axis in the c.m.s. of the observed particles;
- The total longitudinal momentum along the beam axis;
- The total invariant mass (see Fig. 1c);
- The energy within 20° of the missing momentum direction;
- The neutral energy within 15° of the beam axis;
- The number of unassociated track elements in the outer tracking detector within 45° of the missing momentum direction;
- The cosine of the polar angle of the thrust axis.

Prior to the actual analysis, the learning capacity of the network and the number of training cycles are investigated to optimize the performance and to prevent over-training. The number of learning epoques is chosen as 1500. The neural network is then trained on a sample of simulated $q\bar{q}(\gamma)$ events and on a sample of $H^0\nu\bar{\nu}$ events at 55 GeV/c^2, after preselection criteria are applied. The two samples, before preselection, amount to 1.5 million and 3000 events, respectively.

The resulting network is then applied to the real data, to the whole sample of 2.1 million simulated $q\bar{q}$ events and to Monte Carlo samples of the other types of backgrounds,

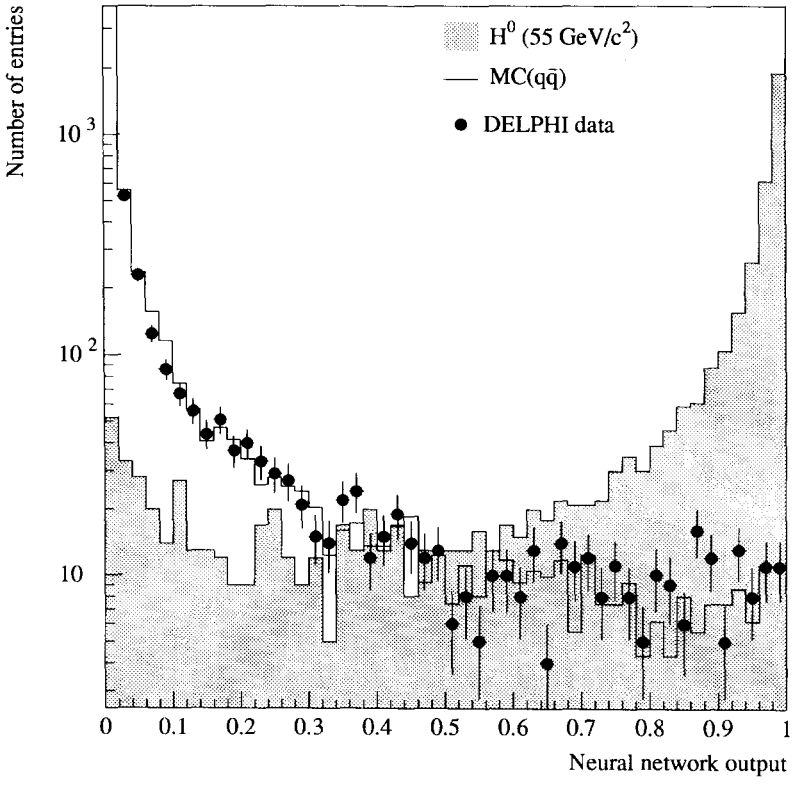

Fig. 2. Distribution of the output of the neural network displaying the separation between the signal and the background. The simulated $q\bar{q}$ events (solid line) are normalised to the data (dots). The shaded area is the expected output for a 55 GeV/c^2 Higgs boson.

such as $\tau^+\tau^-q\bar{q}$ events and two-photon events. For the latter, a sample corresponding to 0.73 times the integrated luminosity is used. The network is also applied to independent reference samples of simulated signal events with different masses of the Higgs particle, to obtain the selection efficiencies. From the study of the rejection power and the selection efficiency of the network, we choose to require the output of the network to be greater than 0.95 for an event to be considered further. This criterion accepts 65.8% of $H^0\nu\bar{\nu}$ events at 55 GeV/c^2 and reduces the background by a factor 430.

As can be seen in Fig. 2, a very good overall separation between background and signal is achieved with the neural network, but it has to be supplemented by additional cuts for sufficient discrimination against the background. These additional selections are defined so that no events remain in the simulated background samples. They are different for events with or without information in the vertex detector.

Table 1
Neural network analysis: effect of the selections on simulated $H^0\nu\bar{\nu}$ events at 55 GeV/c^2, simulated $q\bar{q}$, $\tau^+\tau^-q\bar{q}$ and two-photon events, and real data, for the sample with vertex detector information. The selection efficiency is normalised to the total number of $H^0\nu\bar{\nu}$ events at 55 GeV/c^2 and the various background samples are normalised to the integrated luminosity of the real data sample.

Selection criteria	MC $H^0\nu\bar{\nu}$	MC $q\bar{q}$	MC 4 fermions	MC 2γ	Real data
Preselection	41.6%	2783	4.1	2.8	2342
Network output	26.9%	8.2	0.4	0	7
Quality	26.7%	8.1	0.4	0	6
Impact parameter	25.3%	5.8	0.3	0	3
Acoplanarity	23.4%	2.6	0.1	0	1
S_θ cut	23.1%	2.6	0	0	1
ρ cut	21.0%	0	0	0	0

4.1.2. The sample with vertex detector

The additional selections consist in a quality cut, in the requirement of a b-signature and in three topological cuts. Since events with information in the vertex detector are contained in the barrel region which has good hermeticity, the only possible source of instrumental background is the reconstruction. Events with a significant amount of energy (above 8 GeV) due to reconstruction problems caused by spiraling particles are thus removed.

In order to define the b-signature, the signed impact parameters of the charged particle tracks with respect to the fitted vertex are divided by their errors. The sum of the three largest values is then required to exceed 4. The effect of this criterion was checked on simulated $q\bar{q}$ events. Applying the preselection and the b-tagging condition leads to the following flavour composition in the sample with vertex detector information : 30% of light flavours u, d, s, 20% of $c\bar{c}$ pairs and 50% of $b\bar{b}$ pairs.

The topological cuts are the following:

- The acoplanarity of the two hemispheric jets (see Fig. 1d) is required to exceed 7°;
- The sum of the opening angles of the three pairs of jets when forcing three jets to be reconstructed, S_θ, is required to be less than 358.5°;
- The complement to 180° of the maximum angle between any two jets with energy above 2 GeV, ρ, is required to be greater than 14° in space (see Fig. 1e) and greater than 2° when projected onto the plane transverse to the beam.

These selections eliminate all the simulated backgrounds and leave no event in the data sample. The result is shown in Table 1 where the number of events after each criterion in the selection is given. The selection efficiency for the signal is normalised to the complete sample of simulated $H^0\nu\bar{\nu}$ events at 55 GeV/c^2.

4.1.3. The sample without vertex detector

The background situations differ in the barrel and forward regions. The barrel region has good hermeticity and redundant track information, while the forward region lacks a vertex detector, has incomplete electromagnetic calorimetry in the 40° region and limited detector coverage close to the beam axis. Furthermore, a number of background processes, such as two-photon and beam-gas interactions, mainly populate the forward

Table 2
Neural network analysis: effect of the selections on simulated $H^0\nu\bar{\nu}$ events at 55 GeV/c^2, simulated $q\bar{q}$, $\tau^+\tau^-q\bar{q}$ and two-photon events, and real data, for the sample without vertex detector information. The selection efficiency is normalised to the total number of $H^0\nu\bar{\nu}$ events at 55 GeV/c^2 and the various background samples are normalised to the integrated luminosity of the real data sample.

Selection criteria	MC $H^0\nu\bar{\nu}$	MC $q\bar{q}$	MC 4 fermions	MC 2γ	Real data
Preselection	39.6%	10969	11.8	20.7	10395
Network output	26.5%	22.8	0.6	0	25
Quality	20.6%	13.6	0.4	0	13
P_{miss} activity	19.0%	6.8	0.4	0	8
Acoplanarity	17.7%	2.5	0.4	0	0
S_θ cut	17.5%	2.1	0.1	0	0
ρ cut	17.4%	1.3	0.1	0	0
RMS(p_T)	16.7%	0	0	0	0

region. This makes the background higher in the forward region and leads to a more stringent selection than in the barrel region.

In addition to the reconstruction quality cut mentioned in the previous section, other variables describing energy deposits in the neighbourhood of weak detector regions are included and quality criteria are applied to remove events with lost or badly reconstructed particles:

- The neutral energy deposited within 30° of the beam axis is required to be less than 12 GeV. If the cosine of the polar angle of the thrust axis is between 0.67 and 0.82 a stricter cut of 8 GeV is applied;
- The charged energy deposited within 30° of the beam axis is required to be less than 23 GeV. If the cosine of the polar angle of the thrust axis is between 0.67 and 0.82 a stricter cut of 11 GeV is applied;
- The neutral energy in the 40° region (as measured by the hadronic calorimeter and the electromagnetic calorimeter modules at the edge of the hole) should not exceed 10 GeV;
- The charged energy detected in the 40° region should not be more than 65% of the total charged energy;
- The charged energy within 2° of the plane transverse to the beam (the weak 90° region) must be less than 15 GeV.

Moreover, to ensure that no remaining activity exists in the region pointed at by the missing momentum:

- The total charged and neutral energy contained in a cone with a half opening angle of 20° (40°) around the missing momentum are required to be less than 0.9 GeV (4 GeV);
- The number of unassociated track elements in the outer tracking detector within 45° of the missing momentum direction has to be less than 5.

The following topological cuts are then applied:

- The ratio between the total energies in the two hemispheres must be less than 4;
- The acoplanarity of the two hemispheric jets (see Fig. 1d), must be greater than 8°;
- The sum of the opening angles of the three pairs of jets when forcing three jets to be

Table 3
Neural network analysis: Higgs boson selection efficiency in the neutrino channel as a function of the Higgs boson mass.

m_{H^0} (GeV/c^2)	Efficiency (%)	Statistical uncertainty (%)	Systematic uncertainty (%)
35	34.8	± 1.6	± 1.6
40	40.0	± 1.6	± 1.6
45	44.1	± 1.6	± 1.6
50	42.9	± 0.6	± 1.6
55	37.7	± 0.7	± 1.6
60	28.4	± 0.5	± 1.6
65	16.9	± 0.7	± 1.6
70	8.4	± 0.9	± 1.6

Table 4
Neural network analysis: individual contributions to the systematic uncertainty on the Higgs boson selection efficiency in the neutrino channel.

Uncertainty source	Variation (%)	Systematics (%)
Momentum resolution	see text	0.83
Electromagnetic energy	5.	0.59
Hadronic energy	5.	0.68
Tracking efficiency	5.	0.72
Calorimeter efficiency	5.	0.58
Insensitive region	40.	0.39
Total		1.58

reconstructed, S_θ, is required to be less than 358.5°;
- The complement to 180° to the maximum angle between any two jets with a jet energy above 2 GeV, ρ, (see Fig. 1e) is required to be greater than 7° in space;
- In each hemisphere defined with respect to the plane perpendicular to the sphericity axis in the centre of mass system of the observed charged and neutral particles, the RMS of the distribution of the particle transverse momenta (RMS(p_T)) with respect to the sphericity axis is required to be less than 0.95 GeV/c.

These cuts remove all the simulated backgrounds and leave no candidates in the data. Table 2 shows the number of events surviving at different stages in the analysis. The signal selection efficiency is normalised to the total number of simulated $H^0\nu\bar{\nu}$ events at 55 GeV/c^2.

4.1.4. Final efficiencies and systematic uncertainties

Combining the analyses performed on the samples with and without vertex detector information leads to the total selection efficiencies summarized in Table 3, which also presents the related statistical and systematic uncertainties.

The systematic uncertainties are expected to originate from biases in the reconstructed energies and momenta and in the track reconstruction. Furthermore, an inaccurate de-

scription of the insensitive detector regions in the simulation is also a source of systematic error. The estimation of the individual contributions is carried out by varying the following parameters and evaluating the effect on the selection efficiency:

- The charged particle momenta are smeared according to the experimental momentum resolutions, namely $\delta(1/p) = 0.0008\ (\mathrm{GeV}/c)^{-1}$ in the barrel region and $\delta(1/p) = 0.004\ (\mathrm{GeV}/c)^{-1}$ in the forward region;
- The electromagnetic energy is varied by 5%;
- The hadronic energy is varied by 5%;
- The tracking efficiency is decreased by 5% by randomly dropping tracks;
- The overall calorimeter efficiency is decreased likewise by 5% by randomly dropping neutral showers;
- The insensitive region around 40° is enlarged by approximately 40% and assigned a detection efficiency of 30%.

The results are presented in Table 4. They are independent of the Higgs particle mass. Adding the different contributions in quadrature yields 1.6%.

4.2. Probabilistic analysis

The usual selection method [1,3] based on successive cuts applied to a set of discriminating variables is efficient if the signal and the background are well separated so that the cuts remove most of the background but only a small part of the signal. Otherwise, it is necessary to introduce a large number of different variables with more severe cuts, resulting in a low efficiency for the signal.

The main drawback of this method is that, when events are rejected from one part of the multidimensional space spanned by the discriminating variables, no use is made of the information in other parts of the variable space where there may be an additional separation between signal and background distributions. The second drawback, connected with the former, is that the method of cuts prevents the use of variables for which the signal and background distributions have a large overlap.

For the Higgs boson search in the neutrino channel, such overlaps are expected in many variables. First, inefficiencies in the energy measurement (particle losses or bad reconstruction) tend to smear the distributions. Furthermore, as the Higgs boson mass increases, signal events look more and more like hadronic events. These were the reasons for developing a new analysis method.

4.2.1. Description of the method

The analysis starts by selecting a set of discriminating variables. Each of these variables is then turned into a new variable with the following properties:

(a) The new variable takes its values between 0 and 1;

(b) It has a flat distribution for the background process, i.e. for $q\bar{q}$ events;

(c) It has an asymmetric distribution with an excess below 0.5 for the signal events.

If x refers to the value taken by the initial variable, the new variable is the *probability function* $P(x)$ obtained by integrating the *probability density function* $\rho(t)$ of the initial variable in $q\bar{q}$ *events*. This definition fulfills conditions (a) and (b). Condition (c) is

achieved by integrating $\rho(t)$ over the region where *most of the signal* is expected. As an example, $P(x)$ would be defined by

$$P(x) = \int_{t>x} \rho(t)\,\mathrm{d}t \tag{1}$$

if the signal populates the upper part of the variable distribution. Examples of such variables are the acollinearity of the two hemispheric jets or the missing transverse momentum, as shown in Fig. 1. The probability density function $\rho(t)$ is extracted from the $q\bar{q}$ *background Monte Carlo distributions*, so that $P(x)$ gives the probability to observe a value of the initial variable greater than x in the background process. By construction, the distribution of $P(x)$ is flat for the $q\bar{q}$ background and peaks at low values for the $H^0\nu\bar{\nu}$ signal. Fig. 3 shows the distribution of $P(x)$ for the acollinearity and the missing transverse momentum for real data and simulated $H^0\nu\bar{\nu}$ at 55 GeV/c^2. One can see that the real data distribution can be approximated by a constant, and thus corresponds to the $q\bar{q}$ model, while on the contrary the signal distribution is asymmetric and presents an excess below 0.5.

A global event variable can also be defined, giving the probability for the event to be consistent with the background process. In principle, it should be proportional to the product of all functions $P(x)$ and so be uniformly distributed, provided all variables are uncorrelated. This global variable accumulates all the differences between the signal and the background in the individual variables and gives the possibility to achieve a desired efficiency or purity by applying a single cut. Such an approach has been used to tag b-quarks in hadronic Z^0 decays using as discriminating variables the impact parameters of the charged particles [11].

For the Higgs boson search, the product of the probability functions does not give good discrimination due to the unavoidable correlations between the different variables used in the analysis. Probability functions of correlated variables, when multiplied, give a global probability peaked at low values for the background instead of the expected flat distribution. Events falling in this peak cannot be removed without a large loss in the signal selection efficiency.

In our analysis, a global variable $\mathcal{W}$ is defined instead as the *sum* of the probability functions. Namely, for K selected discriminating variables, labelled by i, we have

$$\mathcal{W} = \sum_{i=1}^{K} P_i(x)\,. \tag{2}$$

For the background, any $P_i(x)$ distribution is flat by definition and for a large number K of uncorrelated variables the distribution of $\mathcal{W}$ should be gaussian with the following mean and variance:

$$\mu_{\mathcal{W}} = K/2\,, \qquad \sigma^2_{\mathcal{W}} = K/12\,. \tag{3}$$

As $\mathcal{W}$ is a sum of probabilities, it is less sensitive to the correlations between the variables and if these are moderate (in practice they do not exceed 0.5), the shape of the $\mathcal{W}$ distribution can, with good accuracy, be approximated by a gaussian. The mean

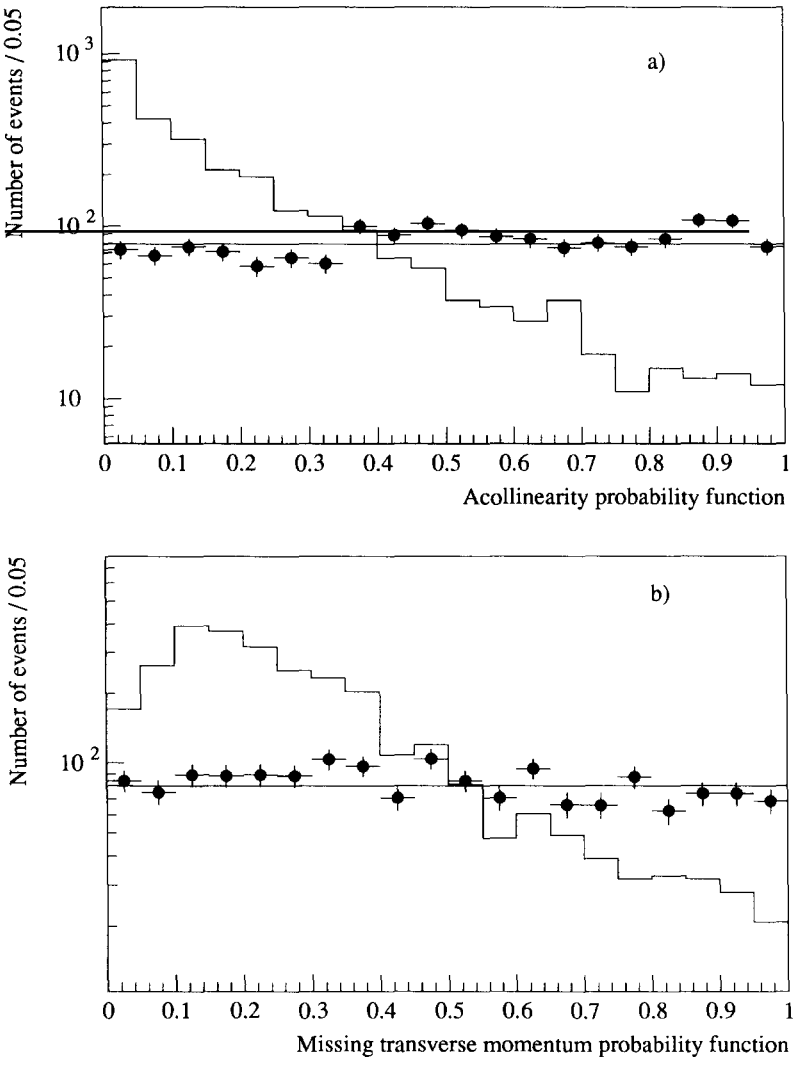

Fig. 3. Probability function distributions of two of the variables used in the probabilistic analysis of the neutrino channel: (a) acollinearity of the two hemispheric jets, (b) missing transverse momentum with respect to the beam axis. The quality and loose preselection cuts described in the text have been applied. Dots stand for real data while the solid line histograms show the expected unnormalised distributions for a 55 GeV/c^2 Higgs boson.

value will be the same as in Eq. (3). The variance will differ from that in Eq. (3) but may still be predicted provided the values of the correlations are known. The weak sensitivity to the correlations of the individual variables and the predictable shape of the distribution for the background process are the two main reasons for using the $\mathcal{W}$

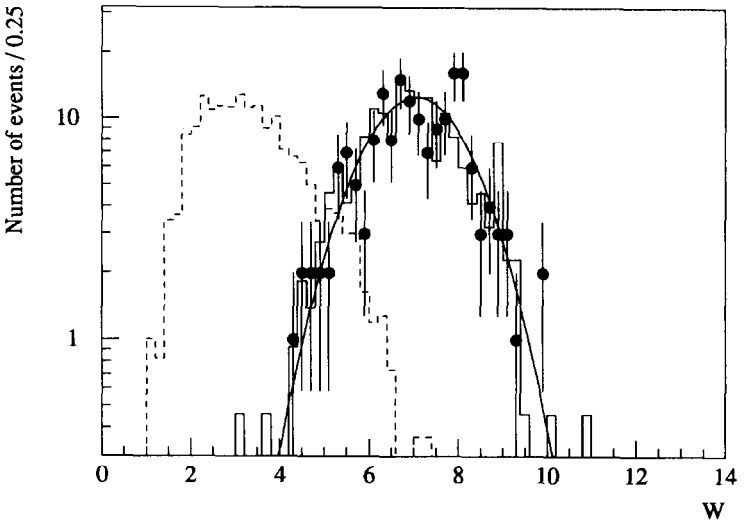

Fig. 4. Distribution of the event global probability $\mathcal{W}$ after quality and preselection criteria (see text), for real data (dots), simulated $q\bar{q}$ events (solid line) and simulated $H^0\nu\bar{\nu}$ events at 55 GeV/c^2 (dashed line). The simulated $q\bar{q}$ sample is normalised to the number of hadronic Z^0 decays in the initial data sample while the normalisation of the signal distribution is arbitrary. The superimposed curve is the result of a fit to the real data distribution by a gaussian.

variable for the Higgs boson search.

For the signal, the shape of the $\mathcal{W}$ distribution cannot be predicted on general grounds but, due to the asymmetry in the distribution of each individual probability function, the $\mathcal{W}$ spectrum is also shifted with respect to the background distribution, accumulating the differences of all discriminating variables.

Fig. 4 shows the $\mathcal{W}$ distribution corresponding to the 14 discriminating variables which enter the probabilistic analysis, as will be described in detail in the following subsections. The background distribution for simulated $q\bar{q}$ events is shown as a solid line histogram, together with the real data (dots). Both distributions are reasonably well fitted by a gaussian while the corresponding distribution for simulated $H^0\nu\bar{\nu}$ events at 55 GeV/c^2 is significantly different. The mean value and the variance both for the real data and the simulated $q\bar{q}$ events agree with the expected values ($\mu_{\mathcal{W}} = 14/2 = 7$, $\sigma_{\mathcal{W}} = \sqrt{14/12} \simeq 1.08$) within the error limits, which means that the effect of the correlations is small.

As the shape of the background distribution is predictable, the expected background remaining in a sample of $\mathcal{N}$ events after a selection on $\mathcal{W}$, $\mathcal{W} < \mathcal{W}_0$, can be estimated as follows:

$$N_{\text{exp}} = \mathcal{N} \cdot \mathrm{G}\left(\frac{\mathcal{W}_0 - \mu_{\mathcal{W}}}{\sigma_{\mathcal{W}}}\right), \qquad G(x) \equiv \frac{1}{\sqrt{2\pi}} \int_{-\infty}^{x} \mathrm{e}^{-t^2/2}\,\mathrm{d}t. \tag{4}$$

For the Higgs boson search, we choose a value of $\mathcal{W}_0$ such that the expected back-

ground in the tail of the simulated $q\bar{q}$ distribution is less than one. This value will be denoted $\mathcal{W}_0(1)$ in the following.

In order to remove the bulk of the background and apply the probabilistic analysis to events which are in the same region of the variable space as the signal, a preselection step is introduced. As a consequence, the cut value $\mathcal{W}_0(1)$ for 1 expected background event increases due to the decrease of the total number of events $\mathcal{N}$. If with such a selection the suppression factor for signal events is much less than for the background, the increase of $\mathcal{W}_0(1)$ can even lead to an overall increase of the selection efficiency.

4.2.2. Quality and preselection criteria

Quality criteria are first applied, in order to discard badly reconstructed events in which some particles are lost in the inefficient regions of the detector. The discriminating variables for these events acquire unexpected values which are strongly correlated and would give a non-gaussian tail in the $\mathcal{W}$ distribution. The quality criteria may be divided in the following groups:

- *Low mass events*: events are rejected if the event mass is less than 30 GeV/c^2 and the transverse momentum is less than 11 GeV/c.
- *Missing particles at* 90°: events are rejected if the missing momentum points at 90° ($|\cos\theta_{\mathrm{mis}}| < 0.1$) and if one of the following conditions is fulfilled:
  - the total electromagnetic energy does not exceed 16% of the total energy,
  - the difference in ϕ between the thrust axis and the missing momentum direction is less than 25°.
- *Missing particles at* 40°: events are rejected if the thrust direction points at the 40° region, as defined in section 3, and if the total charged energy in the corresponding θ range exceeds 11 GeV.
- *Missing particles in forward directions*: events with particles lost in the forward directions comprise the bulk of the background in the neutrino channel. Events are discarded if any of the following conditions is fulfilled:
  - the energy in a 30° (15°) cone around the beam direction is greater than 20 GeV (2 GeV).
  - more than 70% of the neutral energy of the event is deposited in a 30° cone around the beam direction,
  - the missing momentum lies inside a 35° cone around the beam direction and corresponds to more than 35% of the total energy.
- *Quality of the reconstruction* :
  - a large number of hadronic showers not associated to a charged particle track or to a shower in the electromagnetic calorimeter is likely due to noise in the hadronic calorimeter. Events are rejected if the number of unassociated showers in the hadronic calorimeter is greater than 6,
  - hits reconstructed in the outer tracking detector which have not been associated to any track may indicate a lost track. If the number of unassociated hits registered in the outer detector in a 45° cone around the missing momentum is greater than 25, the event is also rejected.

The preselection step consists in requiring the following conditions:

- The event mass is less than 70 GeV/c^2;
- The acollinearity of the two hemispheric jets is greater than 10°;
- The acoplanarity between the two hemispheric jets is greater than 3°. If the jet search gives more than 2 jets, this cut is increased to 10°;
- The absolute value of the cosine of the angle between the thrust direction and the missing momentum direction should be less than 0.95;
- The maximum angle between any two jets is less than 170°;
- The minimum angle between the missing momentum and any jet should be greater than 40°;
- S_θ, the sum of the opening angles of the three pairs of jets, when the event is forced into three jets, is less than 353°;
- The minimal angle between any two jets when the event is forced into three jets should be in the range: $10° < \Theta_{\min} < 90°$.

These selections leave 176 events in the real data sample and 382 simulated $q\bar{q}$ events in a sample of twice as many events. The efficiency for a 55 GeV/c^2 Higgs particle is 48%.

4.2.3. Probabilistic analysis

The remaining events are analysed using the probabilistic method described in section 4.2.1. The complete set of 14 discriminating variables is the following:

- The event mass;
- The event transverse momentum with respect to the beam axis;
- The acollinearity of the two hemispheric jets;
- The acoplanarity of the two hemispheric jets;
- S_θ, as previously defined;
- The sum of the two hemispheric jet masses;
- The minimum opening angle of a cone containing 80% of the event energy;
- The maximum between $|\cos\theta_{\text{mis}}|$ and $|\cos\theta_{\text{thr}}|$ where θ_{mis} (θ_{thr}) is the missing momentum (thrust axis) polar angle;
- The maximum opening angle between any two jets;
- The maximum angle between the directions of any two jets projected onto the transverse plane to the beam;
- The variable σ_{PT} as explained below;
- The missing mass squared;
- The ratio of the total charged energy to the total energy;
- The b-tagging variable L_{PB}, as defined below.

The variable σ_{PT} is defined in the centre of mass system of all observed charged and neutral particles. The sphericity axis of the system is first determined and the event is divided in two hemispheres by a plane perpendicular to this axis. σ_{PT} is defined in the hemisphere with the larger number of particles as the RMS of the distribution of the particle transverse momenta with respect to the sphericity axis.

The variable L_{PB} is the absolute value of the logarithm of the event b-tagging probability defined from the impact parameters of the charged particles. As already mentioned in section 4.2.1, the probabilistic method can also be applied to b-tagging. In that case the

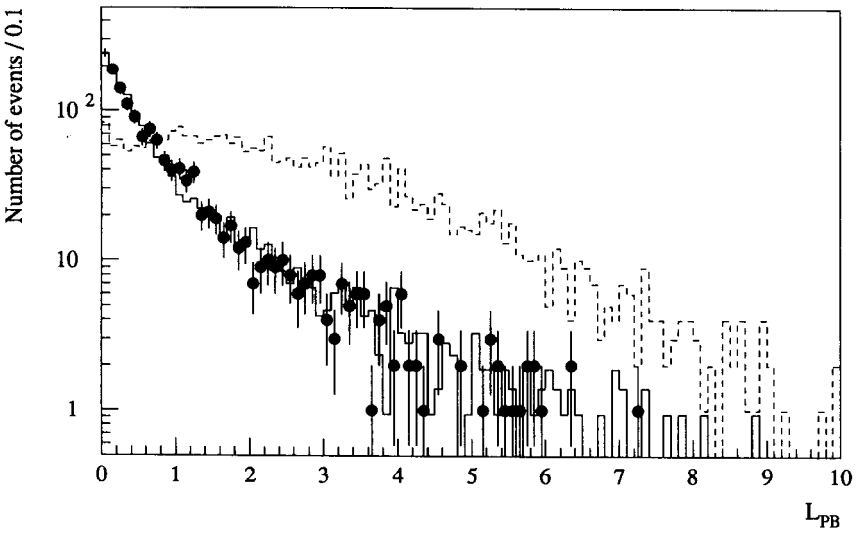

Fig. 5. Distribution of the b-tagging variable, L_{PB}, for real data (dots), simulated $q\bar{q}$ events (solid line) and simulated $H^0\nu\bar{\nu}$ events at 55 GeV/c^2 (dashed line). The quality and loose preselection cuts described in the text have been applied. The simulated $q\bar{q}$ sample is normalised to the number of hadronic decays in the initial data sample while the normalisation of the signal distribution is arbitrary.

discriminant variables are the impact parameters of the charged particles, divided by the related errors. The signal to select is the Z^0 decay into $b\bar{b}$ pairs while the background process consists of the other hadronic decays of the Z^0 boson. As the correlations are low, the event b-tagging probability is computed from the product of the individual probability functions. As is the case for the $\mathcal{W}$ variable, the b-tagging probability measures the probability to obtain the observed values of the discriminant variables in the background process, namely the probability to obtain the observed impact parameters in processes *without b-quarks*. Events containing b-quarks will be characterized by a low probability, typically below 10^{-2}. Fig. 5 shows the distributions of L_{PB} for real data (dots), simulated $q\bar{q}$ (solid line) events and $H^0\nu\bar{\nu}$ events at 55 GeV/c^2 (dashed line). A clear difference is seen between the $H^0\nu\bar{\nu}$ and $q\bar{q}$ processes. On the other hand, a big suppression factor cannot be achieved with any cut on this variable due to the presence of b-quarks in $q\bar{q}$ events and to the limited efficiency of the b-tagging. As an example, a cut on L_{PB} at 2 (3) leads to an efficiency of 34% (20%) and a purity of 86% (95%) on $q\bar{q}$ events. The corresponding selection efficiency is 49% (32%) on $H^0\nu\bar{\nu}$ events at 55 GeV/c^2. So this variable can hardly be used in a standard method with cuts, but it naturally fits in the probabilistic approach.

For each discriminating variable, the probability function $P_i(x)$ is built as described in section 4.2.1 with the corresponding density function computed from the simulated $q\bar{q}$ sample remaining after the preselection step. The distributions of the $\mathcal{W}$ variable calculated from Eq. (2) for the real data and the simulated $q\bar{q}$ and $H^0\nu\bar{\nu}$ events at 55 GeV/c^2 are shown in Fig. 4. The fit to the real data distribution by a gaussian is also shown. The results of the gaussian fits to the real data and simulated $q\bar{q}$ distributions

Table 5
Probabilistic analysis: effect of the selections on simulated $H^0\nu\bar{\nu}$ events at 55 GeV/c^2, simulated $q\bar{q}$, $\tau^+\tau^-q\bar{q}$ and two-photon events, and real data. The simulated background samples are normalised to the number of hadronic Z^0 decays contained in the initial data sample.

Selection criteria	MC $H^0\nu\bar{\nu}$	MC $q\bar{q}$	MC 4 fermions	MC 2γ	Real data
Preselection	73.6%	2944	4.3	138	3262
Quality cuts	62.2%	1005	2.1	4.7	1014
Acoplanarity	55.6%	598	1.7	4.3	603
Min angle thrust/P_{miss}	52.6%	442	0.9	4.0	421
Min angle jet/P_{miss}	50.4%	226	0.5	3.6	210
Min jet/jet angle	48.2%	191	0.2	1.8	176
$\mathcal{W} < 4.$	35.0%	1	0.1	0	0

are the following:

$$\text{real data}: \quad \mu_{\mathcal{W}}^{\text{RD}} = 7.05 \pm 0.08\,, \quad \sigma_{\mathcal{W}}^{\text{RD}} = 1.12 \pm 0.05\,,$$
$$\text{simulated } q\bar{q}: \quad \mu_{\mathcal{W}}^{\text{MC}} = 6.94 \pm 0.06\,, \quad \sigma_{\mathcal{W}}^{\text{MC}} = 1.17 \pm 0.03.$$

The cut limit $\mathcal{W}_0(1)$, computed from the mean value and variance of the gaussian fit to the simulated $q\bar{q}$ distribution is 4.0. Below this limit there is no observed event in the real data. The smallest $\mathcal{W}$ value in this sample is 4.31. The simulated $q\bar{q}$ sample gives two events below the threshold, which corresponds to one event after normalisation to the real data statistics, as expected.

Table 5 shows the effect of the selections on real data, simulated $H^0\nu\bar{\nu}$ events at 55 GeV/c^2 and simulated samples of the background processes: $q\bar{q}$, $\tau^+\tau^-q\bar{q}$ and $\gamma\gamma$ events. For the latter, a sample corresponding to 1.1 times the present integrated luminosity is used. The preselection in the table refers to a subset of the preselection criteria described in the previous section, namely: mass $< 70\,\text{GeV}/c^2$, acollinearity $> 10°$, max jet/jet angle $< 170°$, $S_\theta < 353°$. The effect of each of the remaining preselections is given in the table after the quality cuts are applied. The same loose preselection criteria are used in Figs. 3 and 5.

The Higgs boson selection efficiencies are shown in Table 6 as a function of the boson mass with the related statistical and systematic uncertainties. The latter are estimated from the differences in the gaussian parameters obtained for the real and simulated data, namely: $\mu_{\mathcal{W}}^{\text{RD}} - \mu_{\mathcal{W}}^{\text{MC}} = 0.11 \pm 0.10$, $\sigma_{\mathcal{W}}^{\text{RD}} - \sigma_{\mathcal{W}}^{\text{MC}} = -0.05 \pm 0.06$. Varying the gaussian parameters within these deviations leads to a new value of $\mathcal{W}_0(1)$ and thus to a change in the selection efficiency. Systematic uncertainties around 2% are obtained at each mass, with roughly equal contributions from the shifts in the mean value and in the variance.

The use of a limited data sample to estimate the gaussian parameters $\mu_{\mathcal{W}}^{\text{MC}}$ and $\sigma_{\mathcal{W}}^{\text{MC}}$ leads to an uncertainty in the $q\bar{q}$ background expectation of 1 event. To take this effect into account, the gaussian mean value and variance are varied within the error limits obtained from the fit. This translates into a different number of selected events in the simulated $q\bar{q}$ sample. The difference between this number and one is then taken as the total uncertainty on the one background event expectation. The final expected background from $q\bar{q}$ events is thus 1.0 ± 0.3.

Table 6
Probabilistic analysis: Higgs boson selection efficiency in the neutrino channel as a function of the Higgs boson mass.

m_{H^0} (GeV/c^2)	Efficiency (%)	Statistical uncertainty (%)	Systematic uncertainty (%)
35	35.5	± 1.5	± 1.8
40	41.0	± 1.6	± 1.5
45	41.1	± 1.6	± 1.8
50	38.7	± 0.9	± 1.7
55	35.0	± 0.8	± 1.5
60	25.5	± 0.8	± 1.8
65	14.6	± 1.2	± 2.1
70	6.9	± 0.9	± 1.5

Table 5 shows that four fermion events with taus in the final state also give some background to the Higgs boson search in the neutrino channel. The expected background from this source is found to be 0.13 ± 0.08 (stat) ± 0.02 (syst). The systematic uncertainty on this estimate takes into account a 2% uncertainty on the selection efficiency, a 2% uncertainty on the normalisation and a 15% uncertainty on the four fermion production cross sections.

4.3. Conclusions on the neutrino channel analyses

The neutrino channel is the most difficult one to analyse due to the inherent background in the detection of missing energy. The two independent analyses performed in this channel achieve similar selection efficiencies. The neural network analysis selects no event both in the real data sample and in a sample of 2.1 million simulated background events. This means that less than 1.4 events are expected from the background at the 95% confidence level. On the other hand, the probabilistic analysis selects no event in the real data sample with an expected background of 1.1 ± 0.3 events.

The overlap between the two analyses was checked. About 75% of the selected signal events are common to both analyses. This reflects the fact that the two analyses are different and do not use identical sets of variables so that they select the signal in different regions of the parameter space. A more efficient selection can be achieved by combining the two methods. Table 7 presents the selection efficiencies obtained by keeping events which pass either neutrino analysis. To take into account the correlations between the two analyses, their systematic uncertainties are added linearly to define the systematics uncertainties in the combined analysis.

5. Charged leptonic channels

The experimental signature of a Higgs boson in the charged leptonic channels consists of a pair of isolated and oppositely charged leptons recoiling against a high multiplicity hadronic system. Due to the lepton isolation, different lepton identification criteria can

Table 7
Higgs boson selection efficiencies in the neutrino channel when the neural network and probabilistic analyses are combined.

m_{H^0} (GeV/c^2)	Efficiency (%)	Statistical uncertainty (%)	Systematic uncertainty (%)
35	45.4	± 1.6	± 3.4
40	50.0	± 1.6	± 3.1
45	52.5	± 1.6	± 3.4
50	50.0	± 0.9	± 3.3
55	45.6	± 0.8	± 3.1
60	34.5	± 0.9	± 3.4
65	22.0	± 1.3	± 3.7
70	10.6	± 1.0	± 3.1

be used for the two leptons of a pair, leading to a high dilepton selection efficiency and a small contamination from pions. The main backgrounds in the charged leptonic channels are the semi-leptonic decays of heavy flavour pairs as well as four fermion events with leptons in the final state. Lepton isolation alone rejects almost all of the first background while the dominant contribution from the other is reduced by requiring energetic leptons with a large opening angle and a minimum mass for the rest of the event. Details of the analyses in the electron and muon channels are given in sections 5.2 and 5.3 respectively.

5.1. Dilepton identification

5.1.1. Electron identification

The electron identification combines the information from the electromagnetic calorimeter, the momentum measurement from the tracking devices and the measurement of the energy loss by ionization in the time projection chamber. Two identification levels are defined, referred to as firm and loose tags.

A charged particle is accepted as a firm electron candidate if the corresponding track matches a shower of more than 3 GeV in the electromagnetic calorimeter and the ratio of the shower electromagnetic energy to the track momentum is greater than 0.3. In order to increase the geometrical acceptance of the identification criteria, a charged particle not identified as a muon and pointing to a dead region of the electromagnetic calorimeter is considered as a loose candidate if the energy loss measurement is consistent with what is expected from an electron.

In the Higgs boson search, pairs of charged particles of opposite charges are defined as dielectrons if one is identified as a firm electron and the other as either a firm or a loose electron. If an event contains more than two possible electrons, only the best identified are considered, and among them only the two most energetic ones are kept.

5.1.2. Muon identification

The muon identification relies only on the information provided by the muon chambers. Three identification levels are defined, referred to as loose, standard and tight tags. All tags have been devised with a hadronic environment in mind. The loose tag has the highest efficiency, the standard one is intended to provide a good efficiency with little contamination while the tight tag aims at yielding high purity muon samples.

All tags require a good match in space between the extrapolation of a charged particle's track and the refitted track obtained when muon chamber hits close to the original track are included in the fit. This translates for each tag into different cuts applied to the normalised χ^2 between the extrapolated and fitted tracks. In addition, the standard and tight tags require at least one hit in the muon chamber planes located outside the iron of the hadronic calorimeter, in order to reinforce the selection of penetrating tracks.

The tagging efficiencies for muons above 5 GeV/c produced in hadronic Z^0 decays, as estimated from the simulation, are 85%, 75% and 58% for the loose, standard and tight tags respectively, with misidentification probabilities of hadrons as muons of 1.7%, 1.0% and 0.7%. In the Higgs boson search, the main point is the dimuon identification efficiency. We therefore define as a dimuon candidate any pair of charged particles of opposite charges, with one particle tagged at any of the three levels while the second one has to be either standard or tight.

5.2. Electron channel analysis

A preselection keeps events with at least 6 charged particles of momentum greater than 0.2 GeV/c and coming from the interaction region within 10 cm along the beam direction and within 4 cm in the transverse plane. Two of them must have momenta above 4 GeV/c, opposite charges and have to be classified as a possible dielectron as defined in section 5.1.1.

As the electron energy measurement is affected by radiation losses due to the material in front of the calorimeters, all electron candidates are "dressed" using neutral showers surrounding their trajectories, within some angular range. We use a cut in θ of $\pm 3°$ and an asymmetrical cut in ϕ depending on the track momentum and taking into account the track curvature. The final value of the electron momentum is given by the energy of the dressed shower if it is 1.5 times greater than the track momentum. Otherwise, it is defined as the mean of the track momentum and the dressed shower energy.

In order to specify the event topology, a jet search is made in the hadronic system recoiling from the dielectron using the cluster algorithm LUCLUS [9] with the resolution parameter kept to its default value. The background is then further reduced by requiring the following conditions to be fulfilled:

(a) The energy deposition in the hadronic calorimeter of the firm electron in the dielectron (or any of them if both are firm candidates) does not exceed 5 GeV;

(b) One of the electrons has a momentum above 10 GeV/c while the other has a momentum above 5 GeV/c;

(c) The opening angle between the two electrons is greater than 30°;

Table 8
Effect of the selections on real data, simulated $q\bar{q}$ and $e^+e^-q\bar{q}$ four fermion events and simulated $H^0e^+e^-$ events at 55 GeV/c^2. The background samples are normalised to the number of hadronic Z^0 decays in the initial real data sample.

Selection criteria	Real data	MC $q\bar{q}$	MC 4 fermions	MC $H^0e^+e^-$
Initial sample	924173	924173	12.3	1000
Electron identification	8490	11648	7.6	535
Electron momenta	2448	2608	5.7	486
Isolation angles	44	29	3.4	391
Opening angle	6	2.5	2.5	379
Jet mass	4	2.5	1.3	378
Jet-dielectron angle	3	2.5	1.2	366

(d) The isolation angle with respect to the closest jet is greater than 40° for one electron and greater than 20° for the other;
(e) The angle between the dielectron plane and at least one of the two most energetic jets is greater than 5°, in order to avoid fake jets due to converted photons emitted along the directions of the two electrons;
(f) The invariant mass of the hadronic part of the event is greater than 10 GeV/c^2.

Table 8 summarizes the effect of the selections on real data, simulated $q\bar{q}$ and four fermion events and simulated $H^0e^+e^-$ events at 55 GeV/c^2. The distributions of the main analysis variables are shown in Fig. 6 for real and simulated data. Fig. 6a gives the energy spectrum of the most energetic electron in events passing the preselection, Fig. 6b shows the dielectron opening angle in events passing the preselection and the dielectron identification requirement and Fig. 6c shows the isolation angle of the most isolated electron in the dielectron, in events fulfilling in addition selections b) and c).

A discrepancy between simulated $q\bar{q}$ events and real data appears in table 8 after the electron identification is applied. As shown in Fig. 6a this disagreement is located at low energy in the electron energy spectrum and disappears after the requirement on the electron momenta, as indicated on line 3 of Table 8.

Table 9 shows the signal selection efficiency as a function of the Higgs boson mass with the related statistical and systematic uncertainties. The efficiency drop at high mass is due to the requirement of an energetic electron. As the Higgs boson mass increases, the mass of the recoiling virtual Z^0 boson decreases and so does the energy of the decay electrons. The systematic errors are estimated by varying the selection criteria in the following way:

- Each angular cut is varied by ±1°,
- The cut on the momentum of the most energetic electron is varied between 9 and 11 GeV/c,
- The cut on the momentum of the other electron is varied between 4.4 and 5.6 GeV/c,
- The cut on the ionization loss is varied by ± 1%,
- The recoil mass cut is varied between 7.5 and 15 GeV/c^2.

Three candidates are left in the real data sample. One of them has two well identified isolated electrons in the barrel electromagnetic calorimeter with energies of 32.5 GeV and 16.5 GeV. The most precise estimate of the corresponding Higgs boson mass is

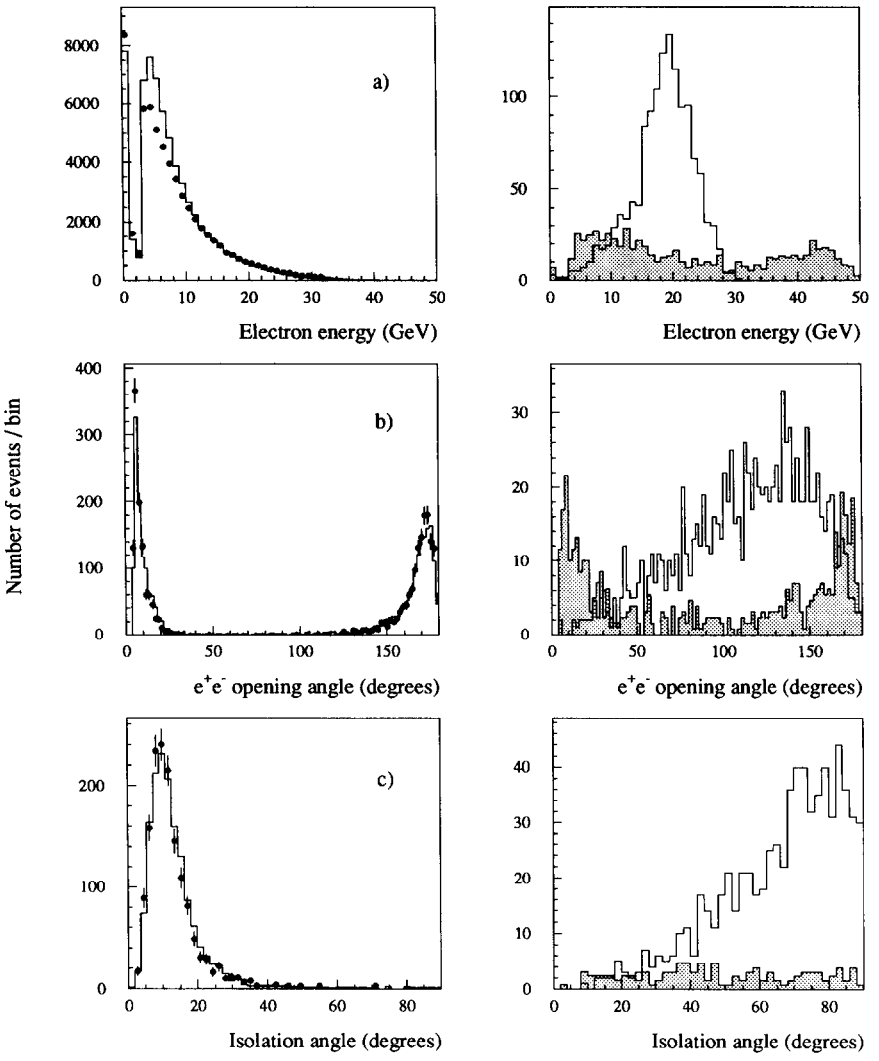

Fig. 6. Distributions of the main variables used in the analysis of the electron channel. Different selections are applied to the three distributions, as described in the text. Plots on the left show a comparison between data (dots) and simulated $q\bar{q}$ events (solid line) normalised to the number of hadronic decays in the initial data sample. Plots on the right show the expected distributions for a 55 GeV/c^2 Higgs boson (solid line, not normalised to the real data) and for four fermions (shaded area, normalised to the initial number of signal events).

obtained after a kinematical fit imposing energy-momentum conservation to the electron and jet four momenta. The fitted mass of this first candidate is found to be $(15.4\ ^{+3.8}_{-3.2})$ GeV/c^2. The second candidate has an electron of 15.2 GeV in the barrel region while the other one has a measured energy in the forward calorimeter of 46.1 GeV, significantly

Table 9
Higgs boson selection efficiency in the electron channel as a function of the Higgs boson mass.

m_{H^0} (GeV/c^2)	Efficiency (%)	Statistical uncertainty (%)	Systematic uncertainty (%)
35	38.5	±1.5	+1.1 −1.7
40	36.9	±1.5	+0.9 −2.3
45	37.2	±1.5	+0.7 −1.6
50	35.6	±1.5	+0.9 −1.6
55	36.6	±1.5	+1.1 −2.3
60	32.4	±1.5	+1.3 −3.0
65	29.8	±1.4	+1.8 −3.5
70	17.1	±1.2	+5.5 −7.5

higher than the momentum measured in the tracking devices, namely 31.6 GeV/c . The fitted mass is (19.2 $^{+3.7}_{-2.3}$) GeV/c^2. The third candidate has electrons of 9.3 GeV and 31.0 GeV, and a mass of (18.9 $^{+4.8}_{-1.9}$) GeV/c^2. The features of these events are summarized in Table 12, which also includes the one candidate from the analysis of the 1990 data sample [1].

Five simulated $q\bar{q}$ events survive the selection in a sample of 1.83 million simulated hadronic Z^0 decays. The electron candidates in these events are either wrongly identified electrons due to the overlap between γ rays from π^0 decays and high energy charged hadrons, or arise from hadronic interactions in the electromagnetic calorimeter leading to high energy photons. The background from $b\bar{b}$ events is included in the previous $q\bar{q}$ sample. Nevertheless, we studied this background source in detail, using simulated $b\bar{b}$ events with the b-quarks decaying semileptonically. No background event was found in a Monte Carlo sample containing as many $b\bar{b}$ pairs as expected with the present integrated luminosity.

Another important background source is the four fermion production with electrons in the final-state, as shown in Table 8. This background is predicted to be 1.17 ± 0.13 (stat) ± 0.18 (syst). The systematic uncertainty on this estimate takes into account a 2% uncertainty on the selection efficiency, a 2% uncertainty on the normalisation and a 15% uncertainty on the four fermion production cross sections.

5.3. *Muon channel analysis*

As a first selection, we require events with at least six charged particles of more than 0.1 GeV/c coming from a region surrounding the collision point within 10 cm along the beam direction and within 5 cm in the transverse plane. Since the muons accompanying the Higgs particle are typically energetic, we select all pairs of oppositely charged particles with momenta greater than 5 GeV/c and with an opening angle greater than 30° in order to suppress the contributions from sequential leptonic decays of b-quarks and from four fermion events with the muon pair arising from the decay of a virtual photon.

We then apply the muon identification criteria to both particles of each selected pair

and keep only dimuon candidates as defined in section 5.1.2. A jet search is applied to the system of particles recoiling from the dimuon, using the cluster algorithm LUCLUS [9] with the resolution parameter kept to its default value. The remaining background is further suppressed by requiring:

(a) the number of jets recoiling against the dimuon to be at least 2;
(b) the missing mass to the dimuon, computed from the muon momenta, to be greater than 15 GeV/c^2;
(c) the visible mass of the system recoiling against the dimuon, to be greater than 10 GeV/c^2;
(d) the momentum of the most energetic muon of the pair, to be greater than 10 GeV/c;
(e) the angle of the most isolated muon of the pair to the closest jet to be greater than 40 °;
(f) the angle of the other muon of the pair to the closest jet to be greater than 20 °.

Selections (a)–(c) provide a strong selection against the four fermion background in which muons come from the decay of a Z^0 boson while quarks are produced from a virtual photon emitted by one of the muons. They also reject any remaining background from tau pairs and radiative muon pairs with hard photons converted in the material of the detector. Selection (d) reduces the background from both $b\bar{b}$ pairs and four fermion events with the muon pair produced by a virtual photon, which are expected to give mostly low momentum muons. Selections (e) and (f) are intended to suppress the remaining $b\bar{b}$ background which leads to muons contained in jets.

Table 10 shows the effect of these successive cuts on the real data sample and on samples of simulated $q\bar{q}$ events, four fermion events with muons in the final-state and $H^0\mu^+\mu^-$ events at 55 GeV/c^2. The difference between the Monte Carlo predictions and the data, as can be seen on line 5 of Table 10, is accounted for by lower muon tagging efficiencies and contaminations in the simulation. The agreement between the real data and simulated $q\bar{q}$ is reasonable: as an example, Figs. 7a–e illustrate the comparison for the variables used in selections (b)–(f), respectively. The preselection criteria and selection (a) have been applied. To illustrate the discriminant power of the analysis variables and the difference between the two main sources of background, Fig. 7 also presents the expected distributions for a 55 GeV/c^2 Higgs particle and for four fermions with muons in the final state.

The selection efficiency as a function of the Higgs boson mass is shown in Table 11 with the related statistical and systematic uncertainties. The selection efficiency is almost independent of the boson mass up to 60 GeV/c^2 and starts decreasing at 65 GeV/c^2 mainly because of selection (d). The systematic uncertainties on the efficiency are evaluated by varying the selection criteria in the following way:

- Each angular cut is varied by ± 1 °,
- The missing mass cut is varied by ± 3 GeV/c^2,
- The recoil mass cut is varied by ± 7 GeV/c^2,
- The cuts on the muon momenta are varied according to the momentum resolution, namely $\delta(1/p) = 0.0008$ $(\mathrm{GeV}/c)^{-1}$ in the barrel region and $\delta(1/p) = 0.004$ $(\mathrm{GeV}/c)^{-1}$ in the forward region.

No variation of the muon identification efficiency is introduced since the simulation leads to underestimated efficiencies.

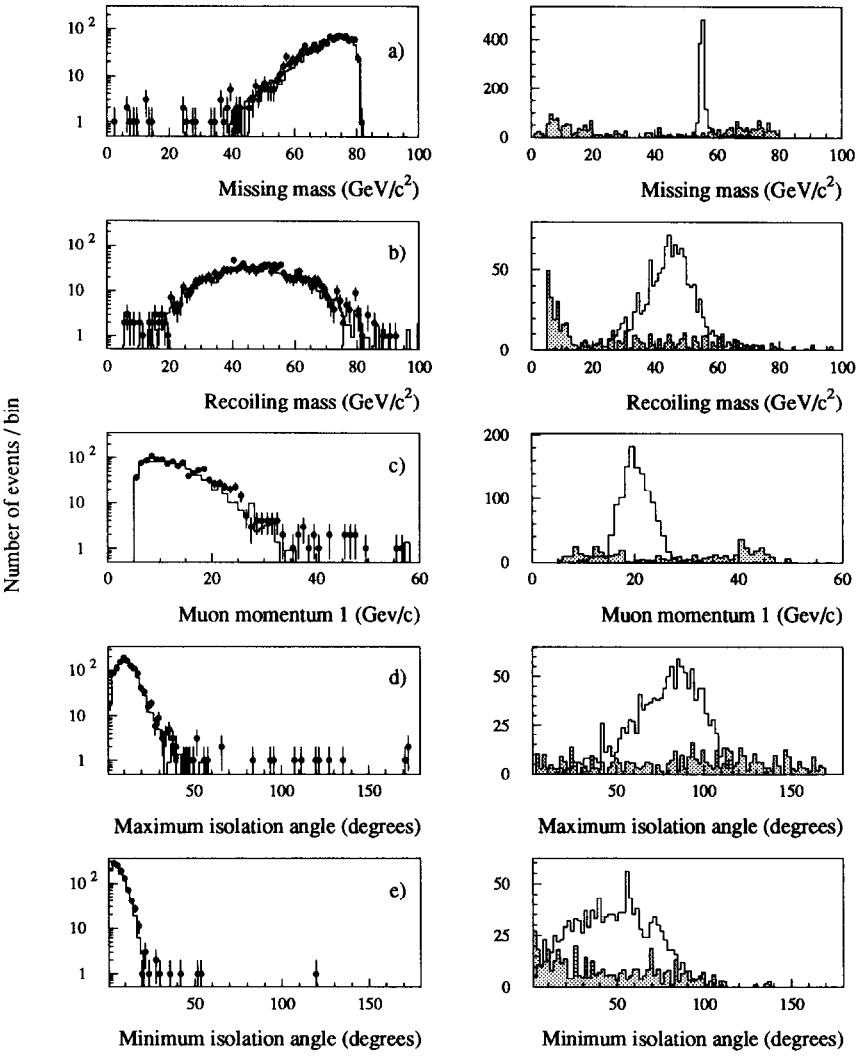

Fig. 7. Distributions of the main variables used in the analysis of the muon channel after the selections described in the text. Plots on the left show a comparison between real data (dots) and simulated $q\bar{q}$ events (solid line) normalised to the number of hadronic decays in the initial data sample. Plots on the right show the expected distributions for a 55 GeV/c^2 Higgs boson (solid line, not normalised to the real data) and for four fermions (shaded area, normalised to 5 times the initial number of signal events except in (a) for which a factor 20 is used for clarity).

Table 10
Effect of the selections on real data, simulated $q\bar{q}$ and $\mu^+\mu^- q\bar{q}$ four fermion events and simulated $H^0\mu^+\mu^-$ events at 55 GeV/c^2. The background samples are normalised to the number of hadronic Z^0 decays in the initial real data sample.

Selection criteria	Real data	MC $q\bar{q}$	MC 4 fermions	MC $H^0\mu^+\mu^-$
Initial sample	983483	983483	103.0	2000
Preselection with dimuon	1233	1087	6.7	1254
nb jets $\geqslant 2$	1206	1087	4.7	1254
Missing mass $\geqslant 15$ GeV/c^2	1195	1087	3.2	1253
Recoil mass $\geqslant 10$ GeV/c^2	1191	1087	3.0	1252
$p_1 \geqslant 10$ GeV/c	792	731	2.4	1250
$\max(\alpha_1^{\text{jet}}, \alpha_2^{\text{jet}}) \geqslant 40°$	5	2.7	1.7	1201
$\min(\alpha_1^{\text{jet}}, \alpha_2^{\text{jet}}) \geqslant 20°$	1	0	1.5	1090

Table 11
Higgs boson selection efficiency in the muon channel as a function of the Higgs boson mass.

m_{H^0} (GeV/c^2)	Efficiency (%)	Statistical uncertainty (%)	Systematic uncertainty (%)
35	54.6	± 1.6	+0.4 −0.8
40	54.3	± 1.6	+0.4 −1.2
45	54.3	± 1.6	+0.3 −0.9
50	52.8	± 1.6	+0.4 −0.7
55	54.5	± 1.1	+0.7 −0.6
60	54.0	± 1.1	+0.7 −0.6
65	48.2	± 1.6	+0.9 −0.8
70	37.7	± 1.5	+1.4 −2.7

As can be seen from Table 10, no event survives the selections in the sample of two million simulated hadronic Z^0 decays. Other sources of background, such as $\mu^+\mu^-(\gamma)$, $\tau^+\tau^-(\gamma)$ events or four fermions with taus in the final state do not contribute to this channel after the selections. At the preselection level after dimuon identification, these backgrounds amount to 8.0, 3.7 and 0.8 events, respectively. After selection (d), they give 0.38, 0.9 and 0.03 events, respectively. These estimates are obtained from samples of simulated muon and tau pairs which correspond to 2.6 and 6.5 times the integrated luminosity. The sample of simulated four fermions with taus in the final state is as presented in the introduction.

One candidate is found in the data, having two well identified, isolated, high energy muons. The corresponding Higgs boson mass, computed from the muon momenta, is 27.8 ± 1.9 GeV/c^2. The event features are summarized in Table 12. Its topology is consistent with what is expected from four fermion events with muons in the final state. This process gives an expected background of 1.48 ± 0.20 (stat) ± 0.23 (syst), in agreement with the observation. The systematic uncertainty on this estimate takes into account a 2% uncertainty on the selection efficiency, a 2% uncertainty on the normalisation and a 15% uncertainty on the four fermion production cross sections.

Table 12
Features of the five events selected in the charged leptonic channels in the whole data sample recorded by the DELPHI experiment from 1990 to 1992. p_1 and p_2 are the lepton momenta, M_{rec} is the recoiling mass from the dilepton, α_1^{jet} and α_2^{jet} are the lepton isolation angles with respect to the closest jet and ω_{ll} is the dilepton opening angle.

Year	Channel	p_1 (GeV/c)	p_2 (GeV/c)	M_{rec}(GeV/c^2)	α_1^{jet}	α_2^{jet}	ω_{ll}
90	e^+e^-	31.5 ± 1.7	21.3 ± 1.4	35.4 ± 5.0	100°	43°	140°
92	e^+e^-	32.5 ± 1.7	16.6 ± 1.2	$15.4\ ^{+3.8}_{-3.2}$	122°	102°	98°
92	e^+e^-	15.2 ± 1.2	46.1 ± 2.0	$19.2\ ^{+3.7}_{-2.3}$	142°	41°	148°
92	e^+e^-	9.3 ± 0.9	31.0 ± 1.7	$18.9\ ^{+4.8}_{-1.9}$	137°	166°	34°
92	$\mu^+\mu^-$	25.1 ± 0.5	18.5 ± 0.4	27.8 ± 1.9	120°	118.5°	56°

5.4. Conclusions on the charged leptonic channels

Due to the large number of events accumulated, the background from hadronic Z^0 decays and four fermion processes is present in the charged leptonic channels. Four events are selected from the sample of 1 million hadronic Z^0 decays recorded in 1991 and 1992, in agreement with the expected background of 2.5 $q\bar{q}$ events and 2.7 four fermion events. The candidate features are summarized in Table 12 which also includes the candidate in the electron channel from the 1990 sample. The recoil masses of the five events are spread over a wide range and do not exceed 40 GeV/c^2. The global b-quark content of the four events in the 1991-1992 sample was checked by applying the probabilistic b-tagging method described in section 4.2.3. None of the candidates is tagged.

As an additional check, Fig. 8 shows a comparison between real data and simulated $q\bar{q}$, $\mu^+\mu^-q\bar{q}$ and $e^+e^-q\bar{q}$ processes with the following loose selections:
- charged multiplicity above 8 (6) in the muon (electron) channel;
- dimuon or dielectron identification;
- lepton momenta above 5 GeV/c ;
- dilepton opening angle above 10°;
- isolation angle of the most isolated lepton above 40°;
- isolation angle of the less isolated lepton above 20°.

A total of 37 events remain in the real data sample while the expected backgrounds are 25.4 $q\bar{q}$ events and 7.6 four fermion events. Radiative leptonic pairs contribute about 0.5 event at the end of these selections and have been ignored in Fig. 8 which shows the mass distribution of the system recoiling against the dilepton, computed from the lepton momenta by requiring energy-momentum conservation. The real data spectrum agrees with the background expectation both in the absolute normalisation and in the shape. Hadronic Z^0 decays are expected to populate the high mass region while four fermion events have a flat distribution over the whole mass range. A study of the other analysis variables shows that, in most of the hadronic events remaining at this point, the dilepton has a low opening angle, as expected from sequential leptonic decays of b-quarks for example. Most of these events are eliminated by the tight selection (greater

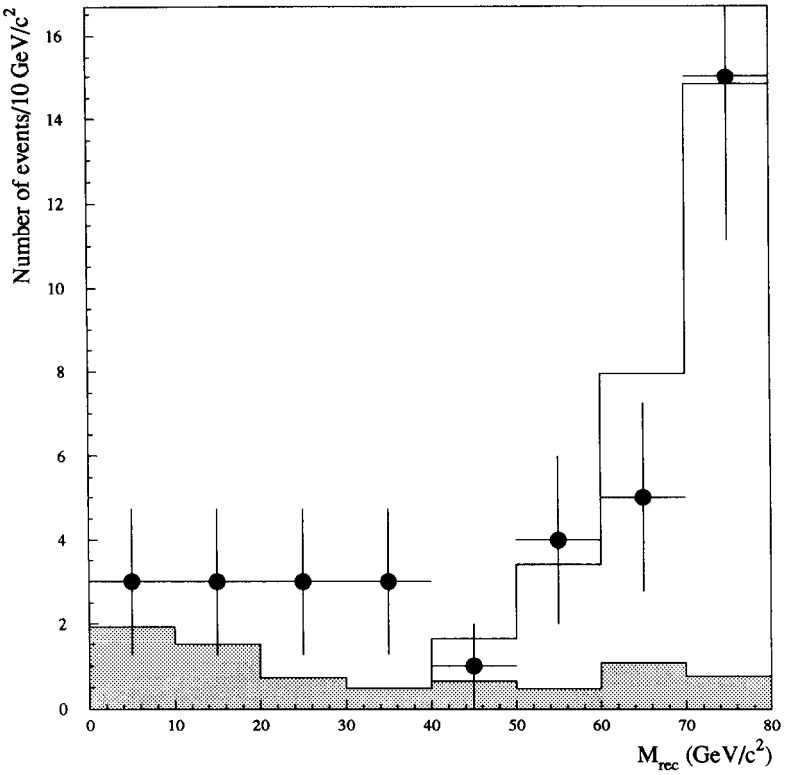

Fig. 8. Mass distribution of the recoiling system from the dilepton in events passing less severe selections than in the analysis. Real data (dots) are compared to the total background expectation from hadronic Z^0 decays and four fermion processes with electrons or muons in the final state (solid line histogram). The shaded area indicates the four fermion contribution.

than 30°) on the opening angle of the dilepton. This is not the case for the remaining four fermion events which have flat distributions in most of the analysis variables, as shown in Figs. 6 and 7, and thus tend to give an irreducible background to the Higgs boson search in the charged leptonic channels.

6. Limit on the mass of the standard model Higgs boson

The search for the standard model Higgs boson in the data sample recorded by the DELPHI detector in 1991 and 1992 identifies four candidate events in the charged leptonic channels. The total expected background from hadronic Z^0 decays and four fermion processes is 6.3 ± 0.5. The four candidates in the charged leptonic channels are scattered in mass and occur in the low mass region where the signal is expected to be a few tens of events. Moreover, there is no evidence of b-quarks in any of them. For these reasons, these four candidates can be attributed to the background.

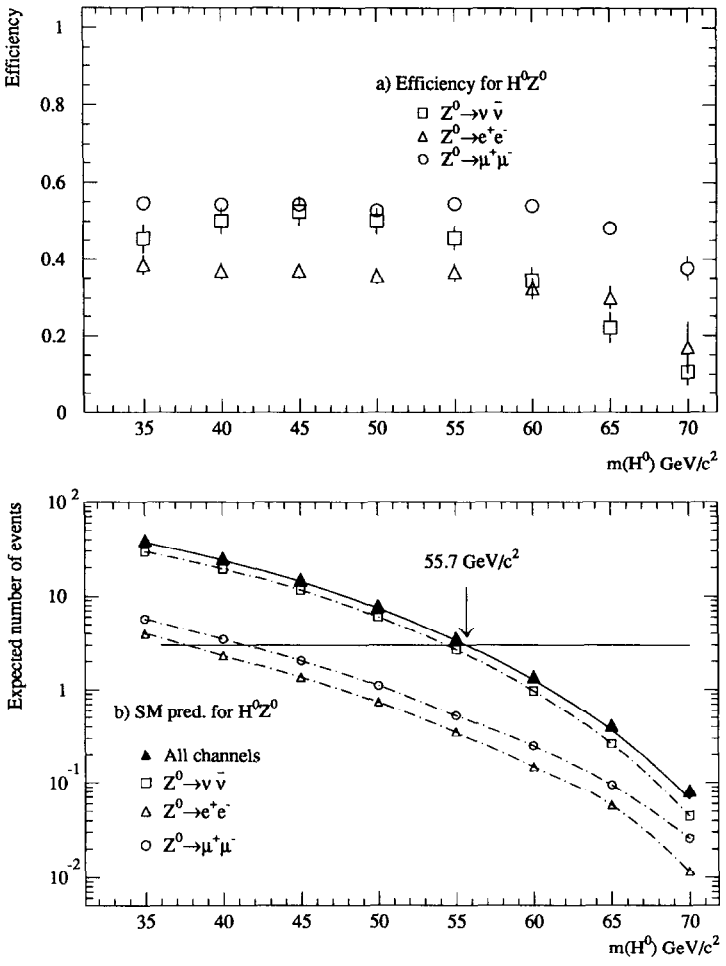

Fig. 9. (a) Higgs boson selection efficiencies as a function of the Higgs boson mass for the analysis performed on 1991 and 1992 data. (b) Expected signal (in the three analysed channels and in total) normalised to the whole data sample recorded by DELPHI from 1990 to 1992. The total expected signal has been decreased by one standard deviation.

This search can be translated into a limit on the Higgs boson mass at the 95% confidence level. For 1991 and 1992 data, the results of the combined analysis in the neutrino channel and the results of the analyses in the electron and muon channels are used. The corresponding efficiencies as a function of the Higgs boson mass are shown in Fig. 9a. The Standard Model parameters obtained from DELPHI data [2] are used to predict the cross sections for the Higgs boson production from the computation of Ref. [12]. This calculation is made in the improved Born approximation with an effective $\alpha(Q^2)$. It includes initial state radiative corrections through exponentiation [13] and a triangle vertex correction [14] with a top quark mass of 200 GeV/c^2. To obtain the expected

signal from the production of a Higgs particle, we use as a conservative normalisation the numbers of hadronic decays recorded during periods where the subdetectors relevant to each analysis were fully operational, that is 966 303, 924 173 and 935 616 hadronic decays for the neutrino, electron and muon channels, respectively. For data taken in 1990, the expected number of events already published [1] is used. It contributes only up to a mass of 50 GeV/c^2.

Before calculating mass limits, the expected number of events is lowered by one standard deviation to allow for the uncertainties on the Higgs boson selection efficiencies presented in the previous sections as well as for the uncertainties on the Higgs boson production cross section and decay branching ratio ($\pm$ 2%) and on the normalisation to hadronic Z^0 decays ($\pm$ 0.5%). All uncertainties are added quadratically. Fig. 9b shows the resulting total expected signal as a function of the Higgs boson mass, together with the 95% confidence level line. The expected signal at a Higgs particle mass of 50, 55, 60 and 65 GeV/c^2 is 7.9 $\pm$ 0.4, 3.6 $\pm$ 0.2, 1.4 $\pm$ 0.1 and 0.41 $\pm$ 0.05, respectively. Thus, comparison of the expected signal with the 95% confidence level restricts the Higgs boson in the framework of the Standard Model to have a mass greater than 55.7 GeV/c^2.

Acknowledgement

We are greatly indebted to our technical collaborators and to the funding agencies for their support in building and operating the DELPHI detector, and to the members of the CERN-SL Division for the excellent performance of the LEP collider.

References

[1] DELPHI Collaboration, P. Abreu et al., Nucl. Phys. B 373 (1992) 3.
[2] DELPHI Collaboration, P. Abreu et al., Nucl. Phys. B 417 (1994) 3; Nucl. Phys. B 418 (1994) 403.
[3] DELPHI note 92-101, PHYS 209, An update on the search for neutral Higgs particles in Z^0 decays (submitted to the Dallas conference).
[4] DELPHI note 93-70, PHYS 297, Search for the Standard Model Higgs boson in Z^0 decays (submitted to the Marseille conference).
[5] ALEPH Collaboration, D. Buskulic et al., Phys. Lett. B 313 (1993) 299;
L3 Collaboration, O. Adriani et al., Phys. Lett. B 303 (1993) 391;
OPAL Collaboration, M.Z. Akrawy et al., Phys. Lett. B 253 (1991) 511.
[6] F.A. Berends and R. Kleiss, Nucl. Phys. B 260 (1985) 32.
[7] F.A. Berends, P.H. Daverveldt and R. Kleiss, Comput. Phys. Commun. 40 (1986) 285, 309.
DELPHI note 91-102, PROG 178, R. Contri, S. Simonetti, Simulation of four massive fermion final states.
[8] DELPHI Collaboration, P. Abreu et al., Nucl. Instrum. Methods A 303 (1991) 233.
[9] T. Sjöstrand, Comput. Phys. Commun. 28 (1983) 227.
[10] L. Lönnblad, C. Peterson and T. Rögnvaldsson, Comput. Phys. Commun. 70 (1992) 167.
[11] ALEPH Collaboration, D. Buskulic et al., Phys. Lett. B 313 (1993) 535.
[12] R.L. Kelly and T. Shimada, Phys. Rev. D 23 (1981) 1940.
[13] G. Burgers, The shape and size of the Z^0 resonance, *in* Polarization at LEP, CERN 88-06, ed. G. Altarelli et al. (1988) 121.
[14] Z. Hioki, Phys. Lett. B 224 (1987) 55.